Received: 8 May 2020 | Revised: 18 June 2020 | Accepted: 23 June 2020

DOI: 10.1096/fj.202001128R

RESEARCH ARTICLE

THE FASEB JOURNAL

Metabolic implication of tigecycline as an efficacious second-line treatment for sorafenib-resistant hepatocellular carcinoma

Martina Meßner[1,2] | Sabine Schmitt[3] | Maximilian A. Ardelt[2] | Thomas Fröhlich[4] | Martin Müller[1] | Helmut Pein[5] | Petra Huber-Cantonati[2] | Carina Ortler[1] | Lars M. Koenig[6] | Lena Zobel[1] | Andreas Koeberle[5,7] | Georg J. Arnold[4] | Simon Rothenfußer[6] | Alexandra K. Kiemer[8] | Alexander L. Gerbes[9] | Hans Zischka[3,10] | Angelika M. Vollmar[1] | Johanna Pachmayr[2]

[1]Department of Pharmacy, Pharmaceutical Biology, Ludwig-Maximilians-University (LMU) Munich, Munich, Germany

[2]Institute of Pharmacy, Center for Public Health, Paracelsus Medical University, Salzburg, Austria

[3]School of Medicine, Institute of Toxicology and Environmental Hygiene, Technical University Munich, Munich, Germany

[4]Laboratory for Functional Genome Analysis (LAFUGA), Gene Centre, LMU Munich, Munich, Germany

[5]Department of Pharmaceutical/Medicinal Chemistry, Institute of Pharmacy, Friedrich-Schiller-University Jena, Jena, Germany

[6]Center of Integrated Protein Science Munich (CIPS-M), Division of Clinical Pharmacology, University Hospital, LMU Munich, Munich, Germany

[7]Michael Popp Research Institute, University of Innsbruck, Innsbruck, Austria

[8]Department of Pharmacy, Pharmaceutical Biology, Saarland University, Saarbrücken, Germany

[9]Department of Medicine 2, Liver Center Munich, University Hospital, LMU Munich, Munich, Germany

[10]Institute of Molecular Toxicology and Pharmacology, Helmholtz Zentrum München, Neuherberg, Germany

Correspondence
Johanna Pachmayr, Institute of Pharmacy, Paracelsus Medical University, Strubergasse 21, 5020 Salzburg, Austria.
Email: johanna.pachmayr@pmu.ac.at

Funding information
Prof. Angelika M. Vollmar was funded by the DFG (VO376/17-1)

Abstract

Sorafenib represents the current standard of care for patients with advanced-stage hepatocellular carcinoma (HCC). However, acquired drug resistance occurs frequently during therapy and is accompanied by rapid tumor regrowth after sorafenib therapy termination. To identify the mechanism of this therapy-limiting growth resumption, we established robust sorafenib resistance HCC cell models that exhibited mitochondrial dysfunction and chemotherapeutic crossresistance. We found a rapid relapse of tumor cell proliferation after sorafenib withdrawal, which was caused by renewal of mitochondrial structures alongside a metabolic switch toward high electron transport system (ETS) activity. The translation-inhibiting antibiotic tigecycline

Abbreviations: AKB, α-ketobutyrate; AKG, α-ketoglutarate; CHA, chloramphenicol; EMT, epithelial-to-mesenchymal transition; ER, endoplasmatic reticulum; ERK, extracellular signal-regulated kinase; ETS, electron transport system; GSEA, gene set enrichment analysis; HCC, hepatocellular carcinoma; IDH2, isocitrate dehydrogenase 2; IMM, inner mitochondrial membrane; MAPK, mitogen-activated protein kinase; mtDNA, mitochondrial DNA; NAD(P), nicotinamide adenine dinucleotide (phosphate); NDUF, NADH-ubiquinone oxidoreductase; nucDNA, nuclear DNA; OAA, oxaloacetate; OGDH, oxoglutarate dehydrogenase; OMM, outer mitochondrial membrane; OS, overall survival; PG, phosphatidylglycerol; PGC-1α, peroxisome proliferator activated receptor gamma coactivator 1 alpha; PI3K, phosphatidylinositol 3-kinase; PYR, pyruvate; ROS, reactive oxygen species; TCA, tricarboxylic acid; TEM, transmission electron microscopy; TGC, tigecycline.

Sabine Schmitt and Maximilian A. Ardelt contributed equally to this study.

impaired the biogenesis of mitochondrial DNA-encoded ETS subunits and limited the electron acceptor turnover required for glutamine oxidation. Thereby, tigecycline prevented the tumor relapse in vitro and in murine xenografts in vivo. These results offer a promising second-line therapeutic approach for advanced-stage HCC patients with progressive disease undergoing sorafenib therapy or treatment interruption due to severe adverse events.

KEYWORDS

antibiotics, electron acceptor auxotrophy, mitochondrial biogenesis, sorafenib resistance, tumor relapse

1 | INTRODUCTION

HCC ranks as the third leading cause of cancer-related mortality worldwide, accounting for more than 700 000 deaths each year.[1,2] The majority of patients are diagnosed with advanced-stage HCC, which is characterized by tumors that have spread beyond the liver, vascular invasion, and cancer-related symptoms.[3] These patients cannot benefit from curative options and are frequently treated with the small molecule sorafenib (Nexavar, Bayer HealthCare Pharmaceuticals-Onyx Pharmaceuticals), an orally administered multikinase inhibitor that exerts antiproliferative, antiangiogenic, and proapoptotic effects.[4] Sorafenib is the first approved systemic therapy for unresectable HCC,[5,6] however, resistance mediated by epithelial-to-mesenchymal transition (EMT) and evasive activation of the PI3K (phosphatidylinositol 3-kinase)/AKT-signaling pathway limits the therapeutic benefit of this drug.[7] In addition, use of sorafenib is hampered by the occurrence of drug-related serious adverse events, which require dose reduction (26%), therapy interruption (44%), or complete abrogation of sorafenib treatment (38%).[5] Importantly, rapid resumption of tumor growth has been previously reported upon withdrawal of tyrosine kinase inhibitors.[7,8] Although tumor relapse represents a major clinical drawback limiting therapeutic effectiveness, the underlying mechanisms remain elusive and there are no therapeutic strategies to address this problem.

Aiming to increase efficacy or safety of HCC therapy, numerous alternative molecular-targeted agents and immunotherapies have been tested in clinical trials since the worldwide approval of sorafenib. However, lenvatinib is non-inferior to sorafenib in a systemic first-line setting and a promising clinical trial of atezolizumab in combination with bevacizumab is still ongoing.[9-11] In the second-line setting, the approval of regorafenib in 2017 represented a breakthrough with a significantly improved overall survival (OS) from 7.8 to 10.6 months. Regardless, because of its strong molecular similarity, a toxicity profile comparable to that of sorafenib was expected. Thus, the RESOURCE trial investigated only patients who were refractory but tolerant to sorafenib.[12] In summary, despite the rapidly developing treatment landscape with newly developed immunotherapy agents,[13] an efficient second-line therapy with a reliable safety profile for sorafenib-intolerant HCC patients remains an unmet but essential need.[14]

To address this problem, we aimed to extend the current knowledge on sorafenib resistance with focus on the mechanistic background of this uncharacterized tumor relapse after sorafenib treatment termination, which might essentially contribute to a poor therapy outcome. Here, we reveal prominent mitochondrial and metabolic alterations in sorafenib-resistant HCC. Moreover, we show that mitochondrial renewal and metabolic reprograming causes rapid resumption of tumor cell proliferation upon sorafenib withdrawal. Importantly, our data demonstrate that this unfavorable relapse of tumor growth can be prevented by inhibiting mitochondrial biosynthesis via the application of translation-inhibiting antibiotics. We thus present an efficacious second-line therapeutic strategy for sorafenib-resistant HCC that may be administered with good clinical experience regardless of the occurrence of sorafenib-associated adverse events.

2 | MATERIALS AND METHODS

2.1 | Cell lines

2.1.1 | Cell authentication

HUH7 cells were obtained from Japanese Collection of Research Bioresources (JCRB0403). RIL175 cells[15] were kindly provided by Prof. Simon Rothenfußer (Center of Integrated Protein Science Munich (CIPS-M) and Division of Clinical Pharmacology, University Hospital, LMU Munich, Germany). CEM/VCR-R cells were characterized[16] and kindly provided by Prof. Maria Kavallaris (University

of New South Wales, Australia). The sorafenib-resistant HUH7-R and RIL175-R cell lines were generated by continuous exposure of HUH7 and RIL-175 cells to increasing concentrations of sorafenib up to 10 μM (BAY 43-9006, Enzo Life Sciences GmbH, Lörrach, Germany). HUH7-R and RIL175-R cells cultured in the presence of 10 μM sorafenib are indicated as HUH7-R(+) and RIL175-R(+) cells. To generate the rebound growth cells HUH7-R(-) and RIL175-R(-), HUH7-R(+), respectively, RIL175-R(+) cells were cultured without sorafenib for 72 hours before seeding if not otherwise indicated.

2.1.2 | Culture conditions

For the cultivation of HUH7 and CEM/VCR-R cells, DMEM (PAN Biotech GmbH, Aidenbach, Germany) and RPMI 1640 (PAN Biotech GmbH, Aidenbach, Germany) supplemented with 10% of FCS (PAA Laboratories GmbH, Pasching, Austria) were used. All cells were cultured at 37°C with 5% of CO_2 in constant humidity. Before cell seeding, culture flasks, multiwell plates, and dishes were coated with collagen G (0.001% in PBS, Biochrom AG, Berlin, Germany).

2.2 | Animal experiments

2.2.1 | Study approval

All experiments were performed according to German respective Austrian legislation of animal protection and approved by: government of Upper Bavaria, Germany: Az 55.2-1-54-2532-22-2016/ Federal ministry of science, research and economy, Austria: BMBWF-66.019-0041-V-3b-2018).

2.2.2 | Mice

For ectopic tumor mouse xenografts female albino SCID "CB17/lcr-PrkdcSCID/lcrlcocrl" mice were used. All mice were purchased between 5 and 6 weeks of age from Charles River.

2.2.3 | Stable lentiviral transfection

Luciferase-positive HUH7 cells (HUH7-R-LUC) were generated by lentiviral transduction using virus supernatant from HEK 293T cells that had been transfected with pCDH-eF-FLuc-T2A-eGFP, pCMV-VSV-G and pCMV-dR8.2 plasmids. Cells were expanded after transduction and sorted for the eGFP-positive population.

2.2.4 | Ectopic tumor mouse xenograft

Mice were shaved on the left lateral abdomen and 3×10^6 cells were injected subcutaneously in the left flank. From the day of tumor cell injection on, mice were treated by intraperitoneal injection with (100 μL solvent: 5% DMSO, 10% solutol, 85% PBS). Three-dimensional tumor size measurement was performed using a digital caliper (Caliper Life Sciences GmbH, Rüsselsheim, Germany) and the tumor volume was calculated.

2.2.5 | In vivo bioluminescence imaging

The size of HUH7-R-LUC tumors was additionally assessed by the IVIS spectrum (Caliper Life Sciences GmbH, Rüsselsheim, Germany). Therefore, 0.3 g/kg mg D-luciferin sodium salt (Biomol GmbH, Hamburg, Germany) dissolved in 100 μL of PBS were injected intraperitoneally in the mice prior to narcotization in 3% of isoflurane. Mice were kept under narcotization with 2% of isoflurane and imaged in lateral position. The bioluminescence signal within the defined region of interest was calculated in photons/second/cm^2 using the Living Image 4.4 software. Images were taken every minute for 20 minutes and the area under the curve (AUC) of luminescence counts was determined. All mice were sacrificed through cervical dislocation and tumors were resected.

2.3 | LC-MS/MS analysis of the cellular proteome and lipidome

2.3.1 | Proteomics analysis

Cells were grown to confluence for 24 hours, washed five times with PBS, detached with trypsin/EDTA and centrifuged (215 rcf, 5 minutes, 4°C). The cell pellets were resuspended in 100 μL of ice-cold PBS and stored at −80°C until further processing. Per 1×10^5 cells 20 μL of 8 M urea/0.4 M NH_4HCO_3 was added. Cells were lysed using an ultrasonic device (Sonoplus GM3200 with BR30 cup booster, Bandelin, Berlin, Germany) applying 10 000 kJ. For further homogenization, samples were centrifuged through QIA-Shredder devices (Qiagen, Hilden, Germany). Protein concentrations were determined by a Bradford assay and adjusted to 0.6 mg/mL with 8 M urea/0.4 M NH_4HCO_3. To cleave bisulfide bonds, 25 μg of total protein was incubated with 1,4-dithioerythritol at a concentration of 4.5 mM for 30 minutes and free sulfhydryl residues were blocked with 10 mM of iodoacetamide for 30 minutes in the dark. After dilution with water to a concentration of 1 M urea, 0.5 μg porcine trypsin (Promega, Madison, WI, USA) was added and incubated overnight at 37°C. Chromatography of peptides was

performed on an EASY-nLC 1000 chromatography system (Thermo Scientific, Waltham, MA) coupled to an Orbitrap XL instrument (Thermo Scientific). Therefore, 2.5 µg of peptides diluted in 0.1% of formic acid (FA) were transferred to a trap column (PepMap100 C18, 75 µm × 2 cm, 3 µm particles, Thermo Scientific) and separated at a flow rate of 200 nl/min (Column: PepMap RSLC C18, 75 µm × 50 cm, 2 µm particles, Thermo Scientific) using a 260 minutes linear gradient from 5% to 25% solvent B (0.1% formic acid, 100% ACN) and a consecutive 60 minutes linear gradient from 25% to 50% solvent B. For data acquisition, a top five data dependent CID method was used.

2.3.2 | Gene set enrichment analysis

For the quantitative analysis of the MS-proteomics data and subsequent volcano plot analysis, the MaxQuant and Perseus software packages (both Max Planck Institute of Biochemistry, Munich) were used. Gene cluster analysis was performed using the gene set enrichment analysis (GSEA) software (The Broad Institute, Massachusetts, USA). Therefore, gene sets were obtained from the Kyoto Encyclopedia of Genes and Genomes (KEGG) (C2.cp.keeg.v.5.1.symbols) and gene ontology database (C5.bp.v.5.1.symbols, C5.cc.v.5.1.symbols, C5.mf.v.5.1.symbols).

2.3.3 | Analysis of fatty acids, phospholipids, and acyl-CoAs

Fatty acids and phospholipids were extracted and analyzed as previously reported.[17] Chromatography was carried out on an Acquity UPLC BEH C8 column (1.7 µm, 1 × 100 mm; Waters, Milford, MA) using an Acquity Ultraperformance LC system (Waters, Eschborn, Germany). Lipids were detected by a QTRAP 5500 mass spectrometer (Sciex, Darmstadt, Germany) equipped with an electrospray ionization source. Glycerophospholipids were identified and quantified in the negative ion mode based on the detection of both fatty acid anion fragments by multiple reaction monitoring (MRM). Sphingomyelins (SMs) were analyzed after fragmentation to the choline head group ($m/z = 184$) by MRM, and free fatty acids were detected by single ion monitoring in the negative ion mode. Absolute lipid amounts were normalized to the internal standard 1,2-dimyristoyl-*sn*-glycero-3-phosphatidylcholine (DMPC) and the cell number. Extraction and analysis of acyl-CoAs was performed using [$^{13}C_3$]-malonyl-CoA as internal standard.[18] In brief, acyl-CoAs were separated on an Acquity UPLC BEH C18 column (1.7 µM, 2.1 × 50 mm) and detected based on the neutral loss of 2′-phospho-ADP ($[M + H\text{-}507]^+$) in the positive ion mode using the UPLC-coupled tandem ESI-MS system described above. Mass spectra were processed using Analyst 1.6 (Sciex, Darmstadt, Germany).

2.4 | Functional analysis of glycolysis and oxidative phosphorylation

2.4.1 | Glycolysis stress test

Cells were seeded into an XFe96 microplate and grown for 24 hours to confluence. The Seahorse Glycolysis Stress Test Kit was used in combination with the Seahorse XFe96 Analyzer (Agilent Technologies, Santa Clara, CA) as described by the manufacturer. Results were normalized to DNA content measured with CyQuant GR dye solution (Thermo Scientific, Waltham, MA) according to the manufacturer's protocol. Data analysis was performed with the Seahorse Wave 2.3.0 software.

2.4.2 | High-resolution respirometry

Mitochondrial oxygen consumption was determined using an OROBOROS Oxygraph-2k (Oroboros Instruments Corp, Innsbruck, Austria). The cells were centrifuged, resuspended in culture medium, and added to the chamber of the oxygraph for stimulation and measurement of the cellular oxygen consumption. Data were analyzed using Datlab 6.1.

2.5 | Microscopy

2.5.1 | Phase-contrast microscopy

The cellular morphology of HUH7-WT and HUH7-R cells (Figure 1A) was assessed under standardized culture conditions using a Leica DMi1 microscope (Leica, Wetzlar, Germany) with a Leica MC120 HD camera (Leica, Wetzlar, Germany). The cellular diameter D (Figure S3A) was assessed by the Vi-Cell XR cell counter (Beckman Coulter, Krefeld, Germany) and used for the calculation of the cellular volume V: $V = 4/3 \times \pi \times D/2$.

2.5.2 | Immunostaining

Cells were seeded in ibidi-µslides (Ibidi GmbH, Martinsried, Germany) and grown overnight. After 24 hours, cells were washed with Ca_2^+/Mg_2^+-containing PBS, fixed with 4% of paraformaldehyde, permeabilized with 1% of Triton-X 100, and incubated with 1% of bovine-serum-albumin (BSA) solution for 30 minutes to block unspecific binding of antibodies. Thereafter cells were incubated with the respective primary

antibody in 0.2% of BSA overnight (4°C): E-Cadherin (HECD1) (1:1000), N-Cadherin (1:200), and PGC-1α (1:300). Cells were washed with PBS and incubated with the secondary antibody together with Hoechst (bisbenzimide H 33342) reagent (1:100) diluted in 0.2% of BSA for 2 hours at RT. The following secondary antibodies diluted in 0.2% of BSA were used: Alexa Fluor 488 goat-anti-mouse IgG (1:400), Alexa Fluor 546 donkey-anti-rabbit IgG (1:400), and Alexa Fluor 488 goat-anti-rabbit (1:400). After washing with PBS, stainings were sealed with mounting medium

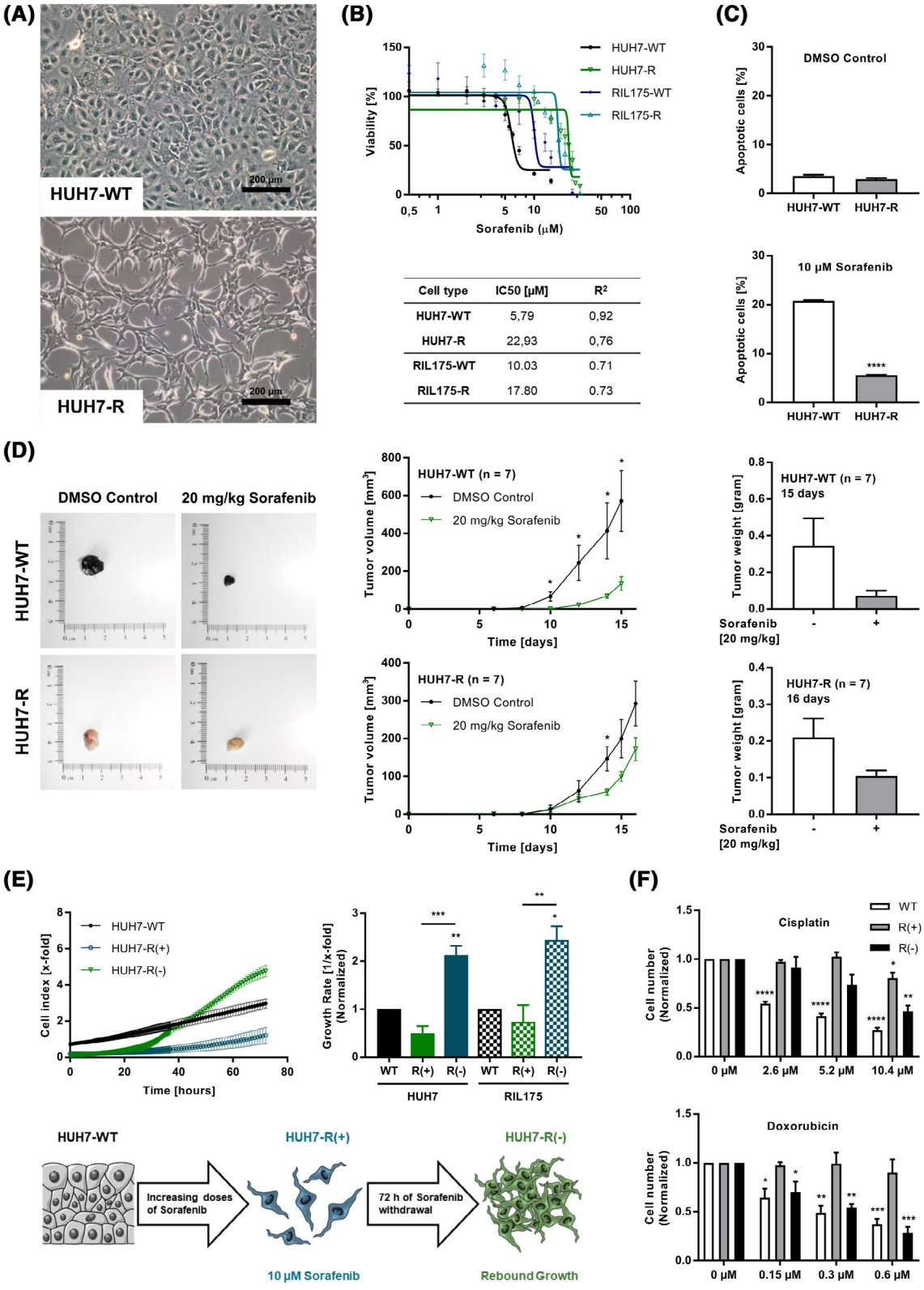

FIGURE 1 The sorafenib-resistant hepatocellular carcinoma (HCC) rebound growth model. A, Mesenchymal phenotype induced by sustained sorafenib exposure. Phase-contrast microscopy of wild-type (HUH7-WT) and sorafenib-resistant (HUH7-R) HUH7 cells. Scale bars indicate 200 µm. B, HUH7-R cells acquired sorafenib resistance to a clinically relevant range. Dose-response curve with corresponding IC_{50}-values and coefficient of determination (R^2) of HUH7-WT, HUH7-R, and wild-type (RIL175-WT), respectively, sorafenib-resistant (RIL175-R) RIL175 HCC cells are shown. C, Sorafenib resistance is sustained after drug withdrawal for 72 hours. Flow cytometric quantification of apoptotic cells (HUH7-WT vs HUH7-R) untreated (top) vs treated with sorafenib for 24 hours (10 µM) (bottom). HUH7-R cells were cultured in sorafenib (10 µM), which was withdrawn for 72 hours prior to stimulation (*t* test). D, HUH7-R cells revealed decreased sorafenib responsiveness in vivo. Ectopic tumor mouse model with HUH7-WT and HUH7-R cell xenografts that were treated with DMSO vs 20 mg/kg sorafenib every second day. Representative excised tumors of the four groups are shown (left) (*t* test). E, Sorafenib withdrawal from HUH7-R and RIL175-R cells continuously cultured in 10 µM of sorafenib (R(+)) leads to significantly increased resumption of proliferation. If not mentioned otherwise, cells with rebound growth were cultured without sorafenib for 72 hours (R(−)). Growth rates were calculated from normalized cell counts (index) obtained by impedance measurements over 72 hours (ANOVA). F, HUH7-R(+) cells acquired reversal chemotherapeutic cross-resistance. Proliferation rates within 72 hours of treatment were normalized to the untreated control (ANOVA). Values are shown as ± SEM, N = 3 for A-C, E-F, N = 7 for D, $*P < .05$, $**P < .01$, $***P < .001$, $****P < .0001$

(FluorSave Reagent) and a cover slip. Samples were kept at 4°C until imaging using a Leica SP8 confocal laser scanning microscope (Leica Microsystems, Wetzlar, Germany).

2.5.3 | Live cell imaging

Mitochondrial morphology and lysosomal mass were assessed in unfixed cells (37°C, 5% CO_2, constant humidity) in a climate chamber (Ibidi GmbH, Martinsried, Germany). Cells were seeded in ibidi-µslides (Ibidi GmbH, Martinsried, Germany) and grown overnight. After 24 hours, cells were washed with PBS and incubated for 30 minutes protected from light with 200 µL/well MitoTracker Green FM (1:9000) or LysoTracker Red DND-99 (1:3000). Images were obtained using a Leica TCS SP8 confocal laser scanning microscope (Leica Microsystems, Wetzlar, Germany) and image analysis was performed with the Leica Application Suite X software. Colocalization of mitochondria and lysosomes (Figure S5B) was quantified using the ImageJ software (National Institutes of Health, Bethesda, MD, USA). Colocalization was manually assessed by calculating the ratio of the yellow area (colocalization) to the total area of green (mitochondria) to red (lysosomes) signals. Further, Pearson's and Manders' (here: green overlapping with red) correlation coefficients were determined as previously described.[19,20] The Pearson's correlation coefficient ranges from +1 (perfect correlation) over 0 (no correlation) to −1 (perfect anti-correlation), whereas for the Manders' split coefficient values range from +1 (perfect correlation) to 0 (no correlation).

2.5.4 | Transmission electron microscopy

After detaching with trypsin/EDTA, 0.5 × 106 cells were centrifuged (200 *g*, 5 minutes, RT) and resuspended in 300 µL PBS. Cells were transferred into 0.95 mL of BEEM capsules (Plano GmbH, Wetzlar, Germany), centrifuged (410 *g*, 10 minutes, RT), and fixed in 600 µL glutaraldehyde (2.5%) in sodium cacodylate buffer (Electron Microscopy Sciences, Hatfield, PA, USA) for at least 24 hours. Thereafter glutaraldehyde was removed and samples were washed three times with 0.1 M of sodium cacodylate buffer, pH 7.4 (Electron Microscopy Sciences, Hatfield, PA, USA). Postfixation and prestaining was done for 45 to 60 minutes with 1% of osmium tetroxide. Samples were washed three times with ddH_2O and dehydrated with an ascending ethanol series (once 15 minutes with 30%, 50%, 70%, 90%, 96%, twice 10 minutes with 100%) and twice 30 minutes with propylene oxide (Serva Electrophoresis GmbH, Heidelberg, Germany). Subsequently, samples were embedded in Epon (3.61 M Glycidether 100, 1.83 M Methylnadicanhydride, 0.92 M Dodecenylsuccinic anhydride, 5.53 mM 2,4,6-Tris-(dimethylaminomethyl)phenol (all reagents obtained from Serva Electrophoresis GmbH, Heidelberg, Germany)). Ultrathin sections were sliced with an Ultramicrotome (Ultracut E; Reichert und Jung, Germany) and automatically stained with UranyLess EM Stain (Electron Microscopy Sciences) and 3% of lead citrate (Leica, Wetzlar, Germany) using the contrasting system Leica EM AC20 (Leica, Wetzlar, Germany). The samples were examined with a JEOL-1200 EXII transmission electron microscope (JEOL GmbH, Freising, Germany).

2.6 | Flow cytometry

For flow cytometry experiments cells were seeded in duplicated and grown overnight and washed with PBS before staining. Analysis and quantification was performed with the FlowJo 7.6 software (Tree Star Inc, Ashland, USA). For stainings of living cells, cell debris was excluded and the fluorescence intensity median normalized to the control. Experiments that compare HUH7-WT and HUH7-R cells were normalized to the cellular volume (Figure S3A).

2.6.1 | Calcein assay

The Multi-Drug Resistance Assay Kit (Calcein AM) (Cayman Chemical, Michigan, USA) was used according to the manufacturer's instructions. Thereby the cells of the positive control were either stimulated with Cyclosporine A (25 μM) or Verapamil (50 μM) and incubated for 30 minutes. The calcein solution provided by the manufacturer was added to the samples in a final concentration of 250 nM and incubated for 30 minutes protected from light. The cells were detached with trypsin/EDTA and transferred in FACS tubes for centrifugation (400 *g*, 5 minutes, 25°C). Fluorescence was assessed on a FACSCanto II (Ex 488 nm, Em 530 nm, Becton Dickinson, Heidelberg, Germany).

2.6.2 | Glucose uptake

Cells were stained with 100 μM of the fluorescent glucose analog 2-(N-(7-Nitrobenz-2-oxa-1,3-diazol-4-yl)Amino)-2-Deoxyglucose (2-NBDG) for 30 minutes protected from light. Thereafter cells were detached with trypsin/EDTA, washed with PBS, and transferred to FACS tubes for centrifugation (400 *g*, 5 minutes, 25°C). Fluorescence was assessed on a FACSCanto II (Ex 488 nm, Em 530 nm, Becton Dickinson, Heidelberg, Germany).

2.6.3 | Cellular superoxides

Cells were incubated for 30 minutes with a 5 μM working solution of the MitoSOX Red dye. The cells were detached with trypsin/EDTA and excess dye removed by centrifugation (400 *g*, 5 minutes, 4°C). The cells were washed, centrifuged again, and kept on ice until measurement on a FACSCalibur (Ex 488 nm, Em 575 nm, Becton Dickinson, Heidelberg, Germany).

2.6.4 | Mitochondrial and lysosomal mass

For assessment of mitochondrial mass, cells were stained with MitoTracker Green FM (1:9000 in DMEM) and for quantification of lysosomal mass, LysoTracker Red DND-99 (1:3000 in DMEM) was used. After incubation for 30 minutes, cells were resuspended in PBS and fluorescence was assessed on a FACSCanto II (Ex 490 nm, Em 516 nm for mitochondrial mass and Ex 577 nm, Em 590 nm for lysosomal mass, Becton Dickinson, Heidelberg, Germany).

2.6.5 | Intracellular Ca^{2+}

Cytosolic calcium levels were determined using the calcium indicator Cal-520 AM (AAT BioQuest, Inc, Sunnyvale, CA, USA) according to the manufacturer's protocol. Cells were incubated with 10 μM of Cal-520 AM (90 minutes, 37°C and 30 minutes, RT). Thereafter cells were detached with trypsin/EDTA, centrifuged (5 minutes, 400 *g*, RT), washed to remove excess dye, and analyzed on a FACSCanto II (Ex 488 nm, Em 530 nm, Becton Dickinson, Heidelberg, Germany).

2.6.6 | Apoptosis analysis

The evaluation of apoptosis rates was performed as described previously.[21] In detail, cells were, trypsinized, washed twice by centrifuging (600 *g*, 10 minutes, 4°C), and resuspended in ice-cold PBS. Next, cells were permeabilized and the DNA stained by adding fluorochrome solution containing propidium iodide (75 μM propidium iodide, 0.1% trisodium citrate, 0.1% Triton X-100, PBS). After an overnight incubation at 4°C, cells were analyzed by flow cytometry on a FACSCalibur (Ex 493 nm, Em 632 nm, Becton Dickinson, Heidelberg, Germany). In apoptotic cells the DNA is fragmented, which results in a sub-G1 peak with low fluorescence, quantified by the FlowJo 7.6 software.

2.7 | Assessment of cell number and proliferation

2.7.1 | Crystal violet staining

For the assessment of cell number, cells were seeded in triplicates in a 96-well plate and grown for 24 hours before stimulation with the test compounds. After an incubation respectively sorafenib withdrawal for 72 hours, the cells were stained for 10 minutes at RT with 100 μM of crystal violet solution (0.5% crystal violet, 20% methanol), before being washed with distilled water. The bound dye was solubilized by adding 200 μL of dissolving buffer (50 mM trisodium citrate, 50% ethanol) and the absorbance was measured at 550 nm on a SpectraFluorPLUS plate-reading photometer (Tecan, Crailsheim, Germany).

2.7.2 | Impedance measurement

The real-time proliferation of HCC cells was assessed using the xCELLigence system (Roche Diagnostics, Mannheim, Germany). The cells were seeded as triplicates in equilibrated 16-well E-plates and incubated for 24 hours before treatment for 72 hours. The cell index, which is proportional to the cell count per well, was assessed through impedance measurement every hour. After normalizing the cell index to the start point of treatment respectively sorafenib withdrawal, the growth rate was calculated by the RTCA software as slope of the cell-index curve.

2.8 | Cellular metabolic activity

2.8.1 | Cell viability

IC50-assessment and growth rescue experiments were determined with the CellTiter-Blue (CTB) Assay (Promega, Mannheim, Germany). Cells were seeded in triplicates into a 96-well plate, stimulated 24 hours after seeding and incubated for 72 hours. For measurement 20 µL of CTB reagent was added to each well with a culture medium volume of 100 µL. After 4 hours of incubation, the metabolic activity, was quantified via dual fluorescence record at 560/590 nm on a SpectraFluorPLUS (Tecan, Crailsheim, Germany) plate reading photometer.

2.8.2 | Intracellular ATP

For the assessment of the cellular dependency toward anaerobic glycolysis, cells were seeded in triplicates in a 96-well plate and grown for 24 hours prior to stimulation with the antimetabolite 2-deoxy-D-glucose (2-DG) (Sigma-Aldrich, Taufkirchen, Germany). After 72 hours, the microplate was equilibrated to RT for 20 minutes and 100 µL of CellTiter-Glo reagent (Promega, Mannheim, Germany) were added to an equal amount of culture medium to each well. For cell line comparisons, cells were seeded in duplicates in a 24-well plate, detached with trypsin/EDTA, normalized in cell number, and incubated with an equal amount of CellTiter-Glo reagent. Cell lysis was induced on an orbital shaker for 2 minutes, following 10 minutes of incubation at RT protected from light. The content of each well was transferred to a white walled Greiner CELLSTAR 96-well plate (Greiner Bio-One International GmbH, Kremsmünster, Austria) and luminescence was recorded with an Orion II microplate luminometer (Berthold Detection Systems, Pforzheim, Germany).

2.8.3 | Lactate fermentation

The extracellular lactate abundance was assessed with the L-Lactate Assay Kit (Cayman Chemical, Michigan, USA) according to the manufacturer's instruction. For each condition 200 µL of supernatant were collected and deproteinated by adding 200 µL of cold 0.5 M metaphosphoric acid provided by the manufacturer, vortexed, and placed for 5 minutes on ice. The samples were centrifuged (10 000 *g*, 5 minutes, 4°C) to pellet the proteins, 360 µL supernatant removed and neutralized with 36 µL of 2.5 M potassium carbonate. In a last centrifugation step (10 000 *g*, 5 minutes, 4°C) precipitated salts were removed and the supernatant used for analysis with the provided detection reagents as described in the manufacturer's protocol. Fluorescence was measured on a SpectraFluorPLUS plate reader (Ex 535 nm, Em 590 nm, Tecan, Crailsheim, Germany).

2.9 | Western blot analysis

Proteins were separated via SDS-PAGE,[22] transferred to a PVDF membrane (Immun-Blot, Bio-Rad, Munich, Germany) and incubated with a primary antibody diluted in 5% of BSA in PBS overnight at 4°C (for details see key resources table): phospho-Akt (Ser473) (1:500; 60 kDa), Akt (1:1000; 60 kDa), phospho-Erk (Thr202/Tyr204) (1:1000; 42/44 kDa), Erk (1:1000; 42/44 kDa), E-Cadherin (1:1000; 135 kDa), Vimentin (1:1000; 57 kDa), Mfn-1 (1:1000; 82 kDa), Drp-1 (1:1000; 78-82 kDa), LC3 (1:1000; 14/16 kDa), phospho-NFKBp65 (Ser536) (1:1000; 65 kDa), NFKBp65 (1:500; 65 kDa), GADD153/CHOP (1:500; ~37 kDa), TFEB (1:1000; 65-70 kDa), TFE3 (1:1000; 72 kDa), Bax (1:500; 23 kDa), Bak (1:1000; 23 kDa), Bcl-2 (1:1000; 26 kDa), PGC-1α (1:1000; ~105 kDa), phospho-AMPK (Thr172) (1:1000; 62 kDa), AMPK (1:1000; 62 kDa), phospho-p38 MAPK (Thr180/Tyr182) (1:1000; 43 kDa), p38 MAPK (1:1000; 40 kDa). For the separation of respiratory chain subunits and TCA-cycle enzymes, electrophoresis was performed with Tricine-PAGE electrophoresis-buffers.[23] The primary antibody mix OxPhos Rodent WB Antibody Cocktail (1:250; 55/48/40/30/20 kDa), IDH2 (1:500; 48 kDa), and OGDH (1:1000; 116 kDa) were used. Proteins were visualized using horseradish peroxidase (HRP) coupled secondary antibodies and ECL solution containing 2.5 mM of luminol. The following secondary antibodies diluted in 5% of BSA in PBS were incubated with the membrane for 2 hours at RT: Goat-anti-rabbit IgG(H + L)-HRP conjugate (1:1000), goat-anti-mouse IgG1-HRP conjugate (1:1000), and donkey-anti-goat IgG-HRP conjugate (1:10 000). Chemiluminescence was detected with the ChemiDoc Touch Imaging system (Bio-Rad, Munich, Germany) and the protein expression was quantified using Stain-free technology and the Image Lab Software. For all quantifications, the protein expression was normalized to the respective protein load and to HUH7-WT.

2.10 | Cellular Redox-balance

2.10.1 | Measurement of NAD^+/NADH and $NADP^+$/NADPH

The NAD^+/NADH and the $NADP^+$/NADPH ratio and total abundance were measured using the commercially available kits NAD/NADH-Glo (Promega, Madison, WI, USA) and NADP/NADPH-Glo (Promega, Madison, WI, USA), respectively. Cells were seeded in triplicates in a 96-well plate and treated as indicated for 72 hours. Extraction and measurement were performed according to the manufacturer's protocol.

Briefly, 60 µL of PBS was added to each well and plates were frozen at −80°C for at least 20 minutes. Cells were scraped off and normalized in protein content by Bradford assay[24] before samples were either left untreated (total NAD, total NADP) or subjected to acid (NAD^+, $NADP^+$) respective basic (NADH, NADPH) treatment. Samples were incubated for 15 minutes at 60°C and pH-neutralized. The luminescence was detected after 60 minutes of incubation in white walled Greiner CELLSTAR 96-well plates (Greiner Bio-One International GmbH, Kremsmünster, Austria) as described by the manufacturer. Luminescence was measured using a Spark multimode microplate reader (Tecan, Crailsheim, Germany).

2.10.2 | Production of reactive oxygen species

Cells were seeded in 96-well plates, grown for 24 hours and treated as indicated. Reactive oxygen species (ROS)-staining and measurement was performed with the ROS Detection Cell-Based Assay Kit (DCFDA) (Cayman Chemical, Michigan, USA) according to the manufacturers protocol. Fluorescence was assessed via dual fluorescence record at 490/530 nm on a Spark multimode microplate reader (Tecan, Crailsheim, Germany). The obtained fluorescence intensities were normalized on cell number by crystal violet staining.

2.11 | Quantitative real-time PCR analysis

For the mRNA isolation from cell culture samples the Qiagen RNeasy Mini Kit (Qiagen, Hilden, Germany) was used according to the manufacturer's protocol. The concentration of mRNA in each sample was determined with the NanoDrop ND 1000 spectrophotomerter (NanoDrop Technologies, Erlangen, Germany) and normalized among the samples. For the creation of cDNA templates the High-Capacity cDNA Reverse Transcription Kit (Applied Biosystems, Foster City, CA) was used as described by the manufacturer. The Real-Time Polymerase chain reaction (RT-PCR) was performed with the QuantStudio 3 Real-Time PCR System (Applied Biosystems, Foster City, CA). SYBR Green Mix I (Applied Biosystems) was used for the RT-PCR of E-cadherin (forward primer: 5′-CAG CAC GTA CAC AGC CCT AA-3′, reverse primer: 5′-AAG ATA CCG GGG GAC ACT CA-3′). For the RT-PCR of PGC-1α the TaqMan Gene Expression Master Mix together with the TaqMan Gene Expression Assay PPARGC1A (Hs00173304_m1, Thermo Scientific) were used.

2.12 | Transient gene-silencing

Gene-silencing experiments were performed with siRNA pools targeting IDH2 (M-004013-00-0005, Dharmacon) and OGDH (M-009679-02-0005, Dharmacon). A nontargeting siRNA for luciferase (siLUC) was used as a negative control (D-001206-14-05, Dharmacon). For transfection the respective siRNA was applied for 1.5 hours in an initial concentration of 50 nM with 0.08% of transfection reagent DharmaFECT 1 (T-2001-02, Dharmacon) per well. The cells were treated as indicated with a final concentration of 25 nM siRNA and 0.04% of DharmaFECT 1 per well. All experiments were carried out 72 hours post transfection.

2.13 | Statistics

All experiments described were conducted at least three times. The data are presented as the mean ± SEM, and statistical significance was considered at $P \leq .05$. Statistical analysis was performed with GraphPad Prism software 7.0. For differences between two groups, an unpaired two-tailed Student's *t* test was used. Group comparisons were performed using one-way ANOVA with Tukey's multiple comparison test.

3 | RESULTS

3.1 | Sorafenib-resistant HCC undergoes a relapse of tumor growth upon sorafenib treatment termination

Although sorafenib is effective at prolonging the median OS of advanced-stage HCC, acquired resistance and tumor relapse has become an obstacle for increasing the life expectancy of patients. To address this clinically highly relevant topic, we generated sorafenib-resistant HCC models by exposing the well-established HCC cell lines HUH7 and RIL175 to increasing doses of the drug. The sorafenib-resistant HUH7-R cells, which are of human origin and obtained resistance up to clinically relevant peak plasma concentrations of 10 µM (human dose: 800 mg/day; 8.5-15.7 µM),[25] were subsequently characterized. We observed a major morphological alteration to a spindle-shaped phenotype (Figure 1A) and distinct chemoresistance up to a half maximal inhibitory concentration (IC_{50}) of 23 µM sorafenib (Figure 1B) that was maintained after treatment termination (Figure 1C). Moreover, the robustness of HUH7-R cells to sorafenib treatment compared to that of their parental HUH7-WT cell line was confirmed in vivo in an ectopic tumor mouse xenograft (Figures 1D, S1A,B).

To mimic the clinical situation of advanced-stage HCC, in which discontinuous dosing schedules are common due to severe adverse events, sorafenib was withdrawn from the cells under standardized conditions. Strikingly, after drug withdrawal from HUH7-R cells cultured in 10 µM of sorafenib (HUH7-R(+) cells), proliferation initially rapidly

resumed within 72 hours. Herein, these cells characterized by a rebound of proliferation are termed HUH7-R(-) cells. This growth relapse upon sorafenib treatment termination was confirmed in RIL175 HCC cells (Figure 1E). Notably, under sorafenib exposure, HUH7-R(+) cells acquired broad cross-resistance to a wide variety of clinically used chemotherapeutics but resensitized after sorafenib withdrawal (Figures 1F, S1C,D). As previously reported, EMT is suggested to contribute to chemoresistance in HUH7-R(+) cells (Figures S1E, S2A-E), which was induced by evasive

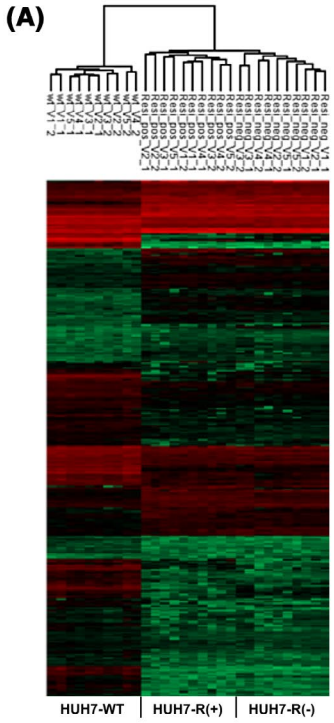

(B)

GENE SET –Enriched in HUH7-WT vs. HUH7-R(+)	SIZE	ES	FDR q-val	NOM p-val
RECEPTOR ACTIVITY	23	-0.6695	0.2604	0.0000
RESPONSE TO CHEMICAL STIMULUS	39	-0.5903	0.4875	0.0055
ENDOPLASMIC RETICULUM	66	-0.5006	1.0000	0.0148
ENZYME ACTIVATOR ACTIVITY	15	-0.6670	1.0000	0.0163
FATTY ACID METABOLISM	20	-0.5957	1.0000	0.0230
ALZHEIMERS DISEASE	48	-0.5046	1.0000	0.0262
MITOCHONDRION ORGANIZATION AND BIOGENESIS	18	-0.6101	1.0000	0.0284
CELLULAR LOCALIZATION	91	-0.4481	0.8513	0.0299
RESPONSE TO STRESS	64	-0.4685	1.0000	0.0314
CYTOPLASMIC PART	317	-0.3821	0.8651	0.0330

GENE SET –Enriched in HUH7-R(+) vs. HUH7-R(-)	SIZE	ES	FDR q-val	NOM p-val
CELL FRACTION	67	0.4082	0.6524	0.0061
MEMBRANE FRACTION	41	0.4566	0.7605	0.0076
CITRATE CYCLE TCA CYCLE	16	0.6149	0.8388	0.0101
ORGANDEVELOPMENT	44	0.3949	0.8651	0.0551
LYSOSOME	22	0.4933	0.9537	0.0574
AMINO SUGAR AND NUCLEOTIDE SUGAR METABOLISM	18	0.5049	0.9361	0.0607
MITOCHONDRION	105	0.3061	0.9706	0.0757
TRANSCRIPTION REPRESSOR ACTIVITY	15	0.5167	0.9649	0.0757
EPITHELIAL CELL SIGNALING IN HELICOBACTER PYLORI INFECTION	15	0.5279	0.7490	0.0772
GLYCOLYSIS GLUCONEOGENESIS	17	0.5040	0.8132	0.0806

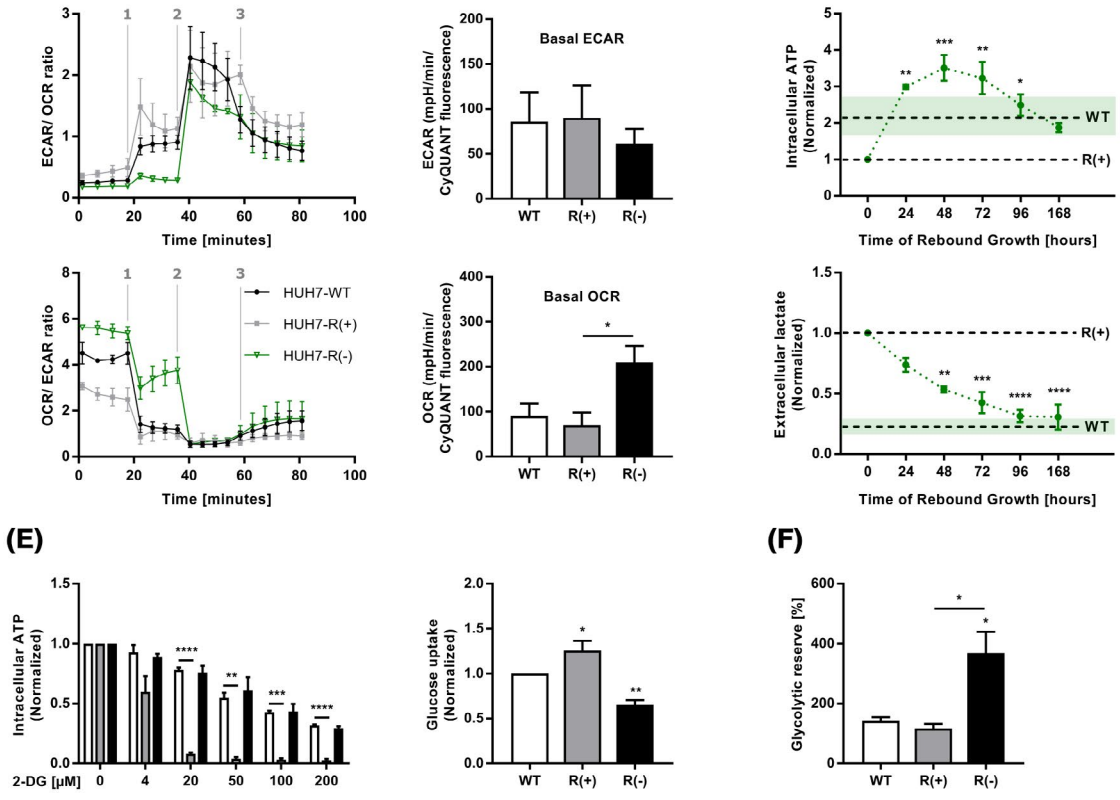

FIGURE 2 MS-based proteomics and metabolic profiling. A, Gene cluster analysis of MS-proteomics screening reveals massive alterations in the proteome of HUH7-R(+) (Resi_pos) and HUH7-R(−) (Resi_neg) cells compared to HUH7-WT (wt). B, Gene sets enriched in HUH7-WT compared to HUH7-R(+) cells (upper panel) and gene sets enriched in HUH7-R(+) compared to HUH7-R(−) cells (lower panel). The top 10 upregulated gene sets of GSEA ranked according to their nominal *P* value (NOM *P*-val) are shown and highlighted for NOM *P*-val < .05. ES: enrichment score, NES: normalized ES, FDR: false discovery rate. C, Metabolic switch from glycolysis to respiration upon rebound growth. The extracellular acidification rate (ECAR) and oxygen consumption rate (OCR) were assessed simultaneously using a glycolytic stress test. Cells were treated with (1) D-glucose (10 mM), (2) oligomycin (1 μM), and (3) 2-deoxy-D-glucose (2-DG) (50 mM). Basal ECAR and OCR were determined at the plateau after D-glucose injection and normalized to the cell number (ANOVA). D, Lactate fermentation and insufficient ATP generation in HUH7-R(+) cells. Measurements were performed upon sorafenib withdrawal and normalized to HUH7-R(+). The mean (dashed line) and SEM (green area) of HUH7-WT cells are shown (ANOVA). E, HUH7-R(+) cells are strongly dependent on glycolysis. ATP levels within 72 hours of glycolysis inhibition by 2-DG were normalized to the untreated control (left). Glucose uptake within 30 minutes was determined by flow cytometry (right) and normalized to HUH7-WT (ANOVA). F, HUH7-R(−) cells have a high capacity to switch from respiration to glycolysis. The glycolytic reserve depicts the percent change in ECAR before and after oligomycin treatment in glycolytic stress test (Figure 2C) (ANOVA). Values are shown as ± SEM, N = 5, technical duplicates for A-B, N = 3 for C-F, **P* < .05, ***P* < .01, ****P* < .001, *****P* < .0001

upregulation of the PI3K/AKT-signaling pathway.[7] In summary, we could confirm that treatment termination after sustained sorafenib therapy causes rapid tumor rebound growth, which will be investigated in this HCC model subsequently.

3.2 | Tumor relapse is accompanied by a metabolic switch toward increased respiratory activity

To obtain better insight into the underlying mechanism of sorafenib resistance and the therapy-limiting tumor relapse, we performed LC-MS/MS-based proteomics screening and identified differentially expressed proteins in HUH7-R cells before and after treatment termination. As sorafenib resistance was accompanied by drastic changes of the cellular proteome, GSEA was applied to elucidate the most prominent altered protein clusters (Figure 2A,B). In HUH7-R(+) cells, GSEA strongly highlighted an elevated abundance of proteins related to mitochondrial structural components and glucose turnover. In addition, higher lysosomal protein expression and suppressed transcriptional activity were observed when compared to HUH7-R(-) cells. Volcano plot analysis at the single-protein level revealed a central role of mitochondrial NADH-ubiquinone oxidoreductase (NDUF) subunit 1, Complex I of the respiratory chain, in HUH7-R(-) cells (Figure S3B-D). The mitochondrial ETS accounts not only for the majority of cellular ATP production, but it also supplies through its Complex I activity mitochondria with the oxidized cofactor NAD^+. In turn, this intrinsic electron acceptor fuels TCA cycle activity, driving biosynthesis, and proliferation.[26,27] Subsequent metabolic profiling by a glycolytic stress test showed that upon growth resumption, HUH7-R cells shift toward a strongly energy-producing phenotype with high oxygen consumption (Figure 2C,D). In contrast, sustained sorafenib exposure was accompanied by an increased rate of lactate fermentation (Figure 2D), an anaerobic high-flux elimination of extra-mitochondrial pyruvate,[28] and a major dependency on anaerobic glycolysis for ATP production (Figure 2E). Upon growth resumption, respiratory active HUH7-R(-) cells displayed the ability to switch to glycolysis after ETS inhibition (Figure 2F). The tendency of cancer cells to undergo aerobic glycolysis and lactate fermentation for energy production, the so-called Warburg effect,[29] has been previously associated with acquired chemoresistance in cancer cells.[30] However, the dependency of HUH7-R(+) cells on anaerobic glycolysis suggests that mitochondrial functionality is impaired.

3.3 | Sustained sorafenib exposure mediates mitochondrial damage and degradation after treatment termination

Prominent alterations in mitochondria and their metabolic pathways, as revealed by LC-MS/MS-based proteomics analysis, warrant a detailed investigation of mitochondrial morphology and its functional dynamics upon tumor growth resumption. Mitochondria form a highly dynamic network undergoing constant fission and fusion to drive metabolism, regulated by dynamin-related protein (Drp1) and marked by mitofusin (Mfn-1) expression on the outer mitochondrial membrane (OMM).[31] A strong increase in mitochondrial mass together with mitochondrial fission was observed in HUH7-R(+) cells compared to HUH7-WT cells, both of which were reversible upon sorafenib withdrawal (Figure 3A). Therefore, sorafenib impaired not only the mitochondrial network, but may also have had an impact on their functionality. First, electron leakage from the ETS led to excessive production of mitochondrial superoxides (O_2^-) in HUH7-R(+) cells, which might

partially be due to the reduced protein expression of respiratory chain subunits Complex I (CI-NDUFB6) and Complex V (CV-ATP5A) (Figure 3B).[32] Second, disrupted mitochondrial functionality was confirmed by low electron transport system (ETS) capacity and routine respiration, as determined by high-resolution respirometry (Figures 3C, S4A). The origin of mitochondrial damage was closely linked to elevated intracellular Ca^{2+} (Figure 3D) and prominent endoplasmic reticulum (ER)-stress, as indicated by NFκB and GADD 153/CHOP activation in HUH7-R cells (Figure S4B,C).[33,34] As

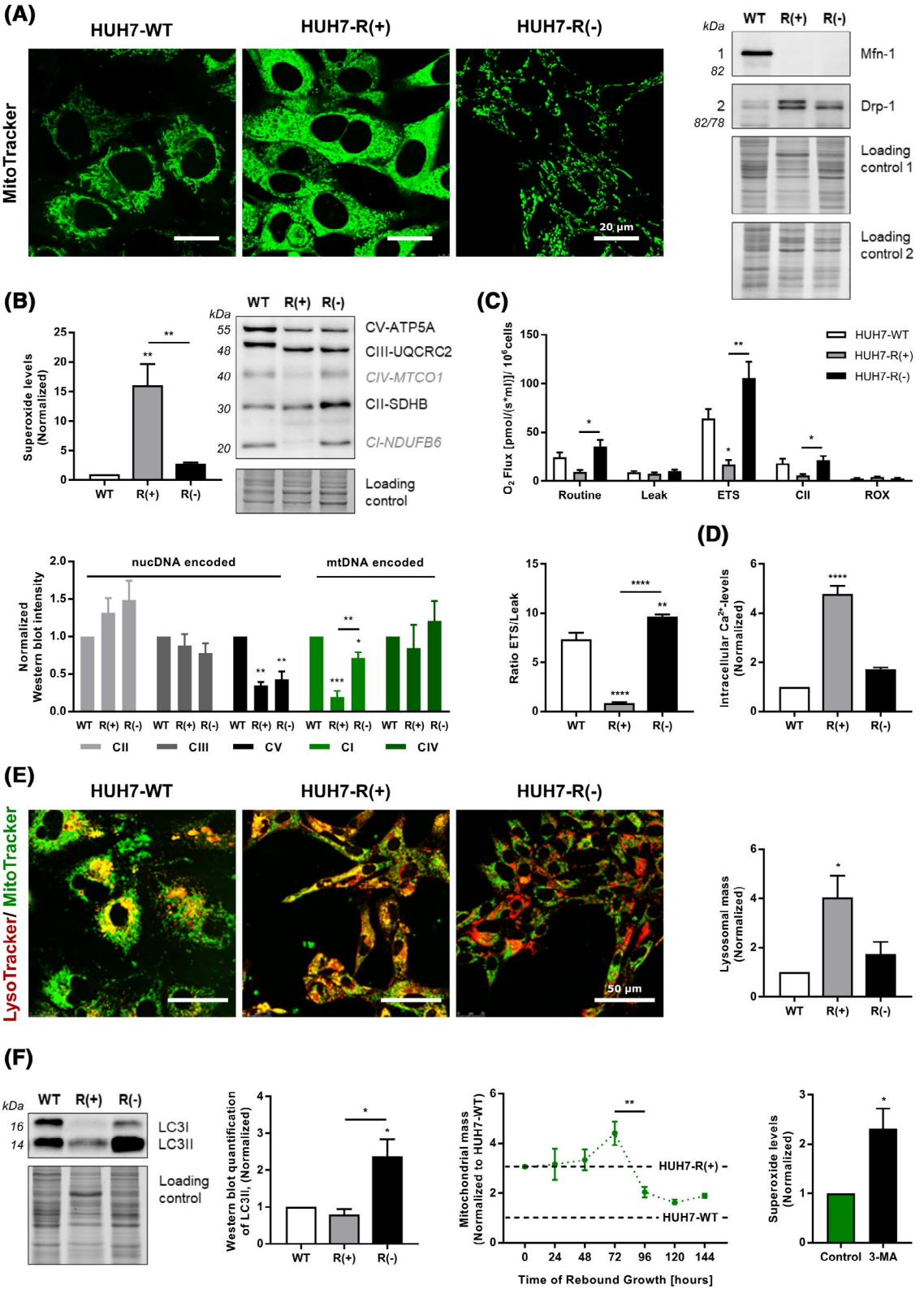

FIGURE 3 Degradation of damaged mitochondria upon tumor relapse. A, Mitochondrial reformation in response to sorafenib. MitoTracker staining of the mitochondrial network (left) and immunoblot analysis Mfn-1 and Drp-1 (right) are shown. Scale bars indicate 20 μm. B, Sorafenib induces damage of the ETS. Flow cytometric quantification of superoxide levels and immunoblot quantification of mtDNA- (CI-NDUFB6, CIV-MTCO1) and nucDNA-encoded ETS-subunits (CII-SDHB, CIII-UQCRC2, CV-ATP5A), both normalized to HUH7-WT (ANOVA). C, Renewed mitochondria acquire increased ETS capacity. High-resolution O_2-flux measurements without treatment (Routine) and after oligomycin (Leak), CCCP (ETS), rotenone (Complex II), and antimycin A (ROX) treatment (method: Figure S4A) (ANOVA). D, High cytosolic Ca^{2+} in HUH7-R(+) cells. Quantification performed by flow cytometry with normalization to HUH7-WT (ANOVA). E, Hints for increased mitophagy and lysosomal biogenesis were observed in HUH7-R(+) cells. Merged images of MitoTracker (green) and LysoTracker (red) live cell staining indicate increased colocalization of mitochondria with lysosomes (yellow) in HUH7-R(+) cells (left panel). Scale bars indicate 50 μm. Flow cytometric quantification of the lysosomal mass was normalized to HUH7-WT cells (right) (ANOVA). See also Figure S5A-C. F, Damaged mitochondria are degraded within 96 hours of rebound growth. Immunoblot quantification for mature autophagosomes (LC3II) was normalized to HUH7-WT (left panel) (ANOVA). Mitochondrial mass (ANOVA) and superoxide levels (t test) were assessed by flow cytometry and normalized to HUH7-WT. For superoxide measurements autophagy was inhibited by 3-methyladenine (3-MA) (5 mM) upon 72 hours of sorafenib withdrawal (right panel). See also Figure S5E. Values are shown as ± SEM, N = 3 for A-B and D-F, N = 4 for C, $*P < .05$, $**P < .01$, $***P < .001$, $****P < .0001$

mitochondria play a critical role in cellular homeostasis, they not only undergo dynamic reformation, but also constant quality control, whereby functionally disturbed mitochondria are engulfed by autophagosomes that fuse with lysosomes for degradation.[35] Hints of mitophagy in HUH7-R(+) cells were previously obtained by GSEA (Figure 2B, lower panel) and supported by increased colocalization of mitochondria with lysosomes and an accumulation of lysosomal mass (Figures 3E, S5A-C). Further, in sorafenib-resistant cells lysosomal biogenesis is induced by the transcriptional activators TFEB and TFE3 (Figure S5D). Nonetheless, due to low levels of LC3II-positive, mature autophagosomes in HUH7-R(+) cells, defective mitochondria were only efficiently degraded at 96 hours after growth resumption, which might contribute to the accumulation of lysosomes in HUH7-R(+) cells (Figures 3F, S5E,F).[35] Thus, inhibition of autophagosome formation upon rebound growth, prevented the degradation of damaged mitochondria and significantly increased superoxide levels (Figure 3F, right panel). Although efficient mitophagy might be impaired in HUH7-R(+) cells, proteasomal removal of OMM proteins Bak, Bcl-2, and previously reported Mfn-1 was observed in HUH7-R cells and prior to sorafenib withdrawal, mitochondrial degradation remained inducible under starvation conditions (Figure S5G,H).[36,37] In summary, we suggest that sorafenib-induced ER stress not only contributes to the unfolding or oxidation of certain OMM proteins, but also leads to an overall impairment of mitochondrial function and consequent removal by the overlapping activity of different mitochondrial degradation pathways.

3.4 | Mitochondria are newly biosynthesized upon growth resumption

Mitochondrial quality control pathways not only eliminate damaged mitochondrial proteins or the entire organelle, but also renew components by adding proteins and lipids through biogenesis, collectively resulting in mitochondrial turnover.[35] Considering that the regeneration of mitochondrial morphology, reestablishment of respiratory functionality and initial increase in mitochondrial mass (Figure 3F) were observed when proliferation resumed, we hypothesized that mitochondrial biogenesis occurs in an early phase after sorafenib withdrawal. Despite damaging mitochondria, elevated intracellular Ca^{2+}-levels-induced protein expression of peroxisome proliferator activated receptor gamma coactivator-1 alpha (PGC-1α), the key regulator of mitochondrial biogenesis, both in vitro and in vivo (Figure 4A,B).[38] PGC-1α is phosphorylated and activated by the cellular energy sensor, AMP-activated protein kinase (AMPK), and p38 MAPK signaling,[39] resulting in nuclear translocation (Figure 4C,D). Transmission electron microscopy (TEM) revealed severe mitochondrial damage in HUH7-R(+) cells and complete mitochondrial recovery within 72 hours of rebound growth. In these newly biosynthesized mitochondria in HUH7-R(-) cells, prominent cristae suggested high respiratory activity (Figure 4E). Mitochondrial biogenesis was also supported by LC-MS/MS-based lipidomics analysis comparing HUH7-R(+) to HUH7-WT cells, which confirmed the strongly reduced fatty acid metabolism indicated by the proteomics screening (Figures 4F, 2B). Lipidomics analysis revealed decreased abundance of all phospholipid subspecies, except for phosphatidylglycerol (PG), which was significantly increased in HUH7-R(+) cells. PG is the precursor of cardiolipin, which is exclusively integrated into the inner mitochondrial membrane (IMM), where it acts as an essential constituent that contributes to crista formation and energy conversion via respiration; cardiolipin thus represents a hallmark lipid of mitochondrial biogenesis.[40] Given that sustained sorafenib exposure has been shown to impair the functionality of ETS subunits required to fuel tumor relapse, inhibition of mitochondrial renewal evoked as a potential target for second-line therapies after sorafenib therapy termination.

3.5 | Tigecycline (TGC) impairs rebound growth in vitro by establishing auxotrophy for electron acceptors

According to the endosymbiont hypothesis, mitochondria are derived from α-proteobacteria that were enveloped by pre-eukaryotic cells, providing an additional energy source and thereby conferring a competitive advantage.[41] Notably, mitochondrial ETS subunits are partially encoded by both nuclear (nucDNA) and prokaryotic-derived mitochondrial DNA (mtDNA).[42] We hypothesized that suppressing biogenesis of mtDNA-encoded subunits by bacterial translation-inhibiting

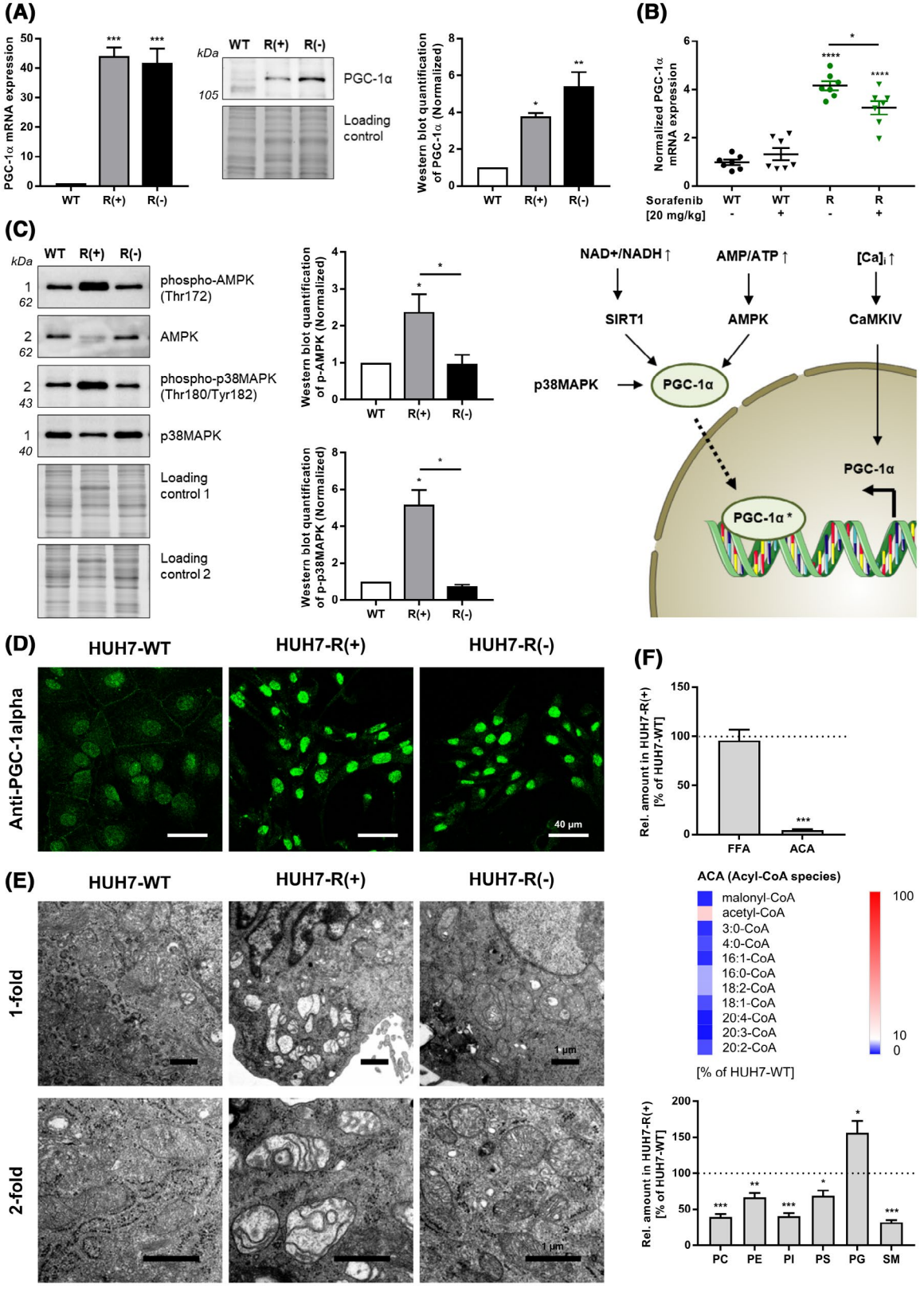

FIGURE 4 Mitochondrial biogenesis induced by PGC-1α. A, Elevated PGC-1α abundance in HUH7-R cells. mRNA-levels (left) and immunoblot quantification (right) of PGC-1α were normalized to HUH7-WT (ANOVA). B, Sorafenib modifies PGC-1α mRNA expression in HUH7-R cells in vivo. PGC-1α mRNA levels in excised tumors of ectopic mouse xenografts (Figure 1D) are normalized to the mean of HUH7-WT expression (ANOVA). C, Induction of AMPK- and p38MAPK-signaling for PGC-1α activation. Immunoblot quantification of phospho-AMPK and phospho-p38MAPK normalized to HUH7-WT (ANOVA) and schematic illustration of the PGC-1α activation cascade for induction of mitochondrial biogenesis is shown. D, Nuclear translocation of PGC-1α is shown by immunostaining. Scale bars indicate 40 μm. E, Mitochondrial damage and regeneration after sorafenib withdrawal is shown by TEM. Scale bars indicate 1 μm. F, Increase in PG-levels, despite breakdown of fatty acid synthesis in HUH7-R(+). MS-based lipidomics with normalization of free fatty acid (FFA), Acyl-Co-A species (ACA), phosphatidylcholine (PC), phosphatidylethanolamine (PE), phosphatidylinositol (PI), phosphatidylserine (PS), phosphatidylglycerol (PG), and sphingomyelin (SM) abundance to HUH7-WT. The heatmap is color coded from blue (0%) to white (10%) to red (100%) (top: t test, bottom: ANOVA). Values are shown as ± SEM, N = 3 for A-E, N = 5 for F, $*P < .05$, $**P < .01$, $***P < .001$, $****P < .0001$

antibiotics would block the metabolic switch of HUH7-R and RIL175-R cells when released from sustained sorafenib treatment. Indeed, TGC impaired the biogenesis of mtDNA-encoded subunits CI-NDUFB6 and CIV-MTCO1, thereby abrogating the recurrence of tumor growth (Figure 5A,B). At a TGC concentration (25 μM) that significantly impaired cell proliferation but did not induce apoptosis, concomitant reduction in NAD^+ recovery and increased lactate fermentation were observed, whereas cellular ATP levels remained unaffected (Figure 5C). Therefore, growth resumption appears to be limited by the reduction in aerobic glycolysis through a diminished NAD^+/NADH ratio rather than by the cell's energetic state. Both the abrogation of tumor relapse and the increase in anaerobic glycolysis were confirmed by the antibiotic chloramphenicol (CHA) in this setting (Figure S6A-C). Next, we performed rescue experiments with various TCA cycle intermediates to determine the limiting precursors required upon tumor relapse. Surprisingly, among the metabolites tested, only pyruvate (PYR), α-ketoglutarate (AKG), and oxaloacetate (OAA) sufficiently restored proliferation by reversing NAD^+ depletion, whereas no rebound growth rescue was observed with acetyl-CoA, malate, citrate, cysteine, or aspartate (Figure 5D, S6D). We hypothesized a structural causality of successful growth rescue as the alpha-ketoacids PYR, AKG, and OAA are substrates of NAD^+-regenerating dehydrogenases (Figure 5E). To uncouple the role of TCA cycle intermediates as NAD^+-regenerating electron acceptors from their role as carbon sources for cellular biogenesis, we supplemented TGC-treated HUH7-R cells after sorafenib withdrawal with α-ketobutyrate (AKB), which is not part of the TCA cycle. As shown previously, AKB acts as a substrate of dehydrogenases, oxidizing NADH to NAD^+ while supplying cells with neither carbon nor ATP.[26,43] Indeed, AKB successfully restored HUH7-R cell proliferation to a similar extent as PYR, AKG, and OAA (Figures 5D,E, S6D). Altogether, these data suggest that inhibited biogenesis of mtDNA-encoded ETS subunits under TGC treatment leads to impaired NAD^+ recovery by the NDUF, diminishing aerobic glycolysis in HUH7-R cells upon sorafenib withdrawal. These key results were confirmed in RIL175-R cells (Figure S7). Thus, upon TGC treatment cells suffer reductive stress, which renders the exogenous electron acceptor supply limiting for restoring rebound growth.

3.6 | Abrogation of tumor relapse-fueling oxidative glutamine metabolism by TGC leads to sustained mitochondrial damage

Next, we aimed to investigate in detail how diminished NAD^+/NADH recovery under TGC treatment affects oxidative processes and prevents HUH7-R cells from resuming proliferation. It is known that despite the presence of glucose, glutamine is one of the most consumed nutrients to fuel oxidative TCA cycle activity, thus, contributing to cellular energy generation and biosynthesis.[44] To analyze the contributions of glucose and glutamine to tumor relapse, we transiently silenced oxoglutarate dehydrogenase (OGDH) downstream of the oxidative glutamine pathway and isocitrate dehydrogenase (IDH2) downstream of glucose, but upstream of glutamine oxidation (Figure 6A,B). Interestingly, suppression of OGDH expression impaired rebound growth and diminished the NAD^+/NADH ratio of HUH7-R cells upon sorafenib withdrawal, whereas IDH2 silencing per se did not have an effect (Figure 6C). In addition, OGDH protein levels were significantly increased in HUH7-R(-) cells, supporting glutamine oxidation as a driving force for rebound growth (Figures 6D, S8A). The ETS is substantially powered by NADH provided by the oxidative TCA cycle,[44] thus, NDUF activity is impaired by both TGC treatment and OGDH silencing. In turn, the NDUF provides electron acceptors for de novo aspartate synthesis using glutamine carbon.[26] Although we confirmed that TGC hinders aspartate production, levels of this amino acid were not limiting for rebound growth (Figure S8B,C). However, TCA cycle-derived aspartate or malate is exported to the cytoplasm and converted to pyruvate to produce NADPH (Figure S8D,E).[45] NADPH is an electron donor for biosynthetic processes that can transfer its reducing potential to glutathione (GSSG) for ROS elimination.[32] In fact, ROS levels were elevated by

both OGDH silencing and TGC treatment and rescued by the ROS-scavenger N-acetyl cysteine (NAC) (Figure 6E). Furthermore, impaired maintenance of redox homeostasis was confirmed in HUH7-R(+) cells and by CHA treatment upon growth resumption (Figure S8F). Thus, defective elimination of ROS by TGC treatment or abrogation of glutamine oxidation by OGDH silencing alters the integrity of mitochondrial cristae, which might not only prevent tumor relapse, but also contribute to a long-term treatment benefit (Figure 6F).

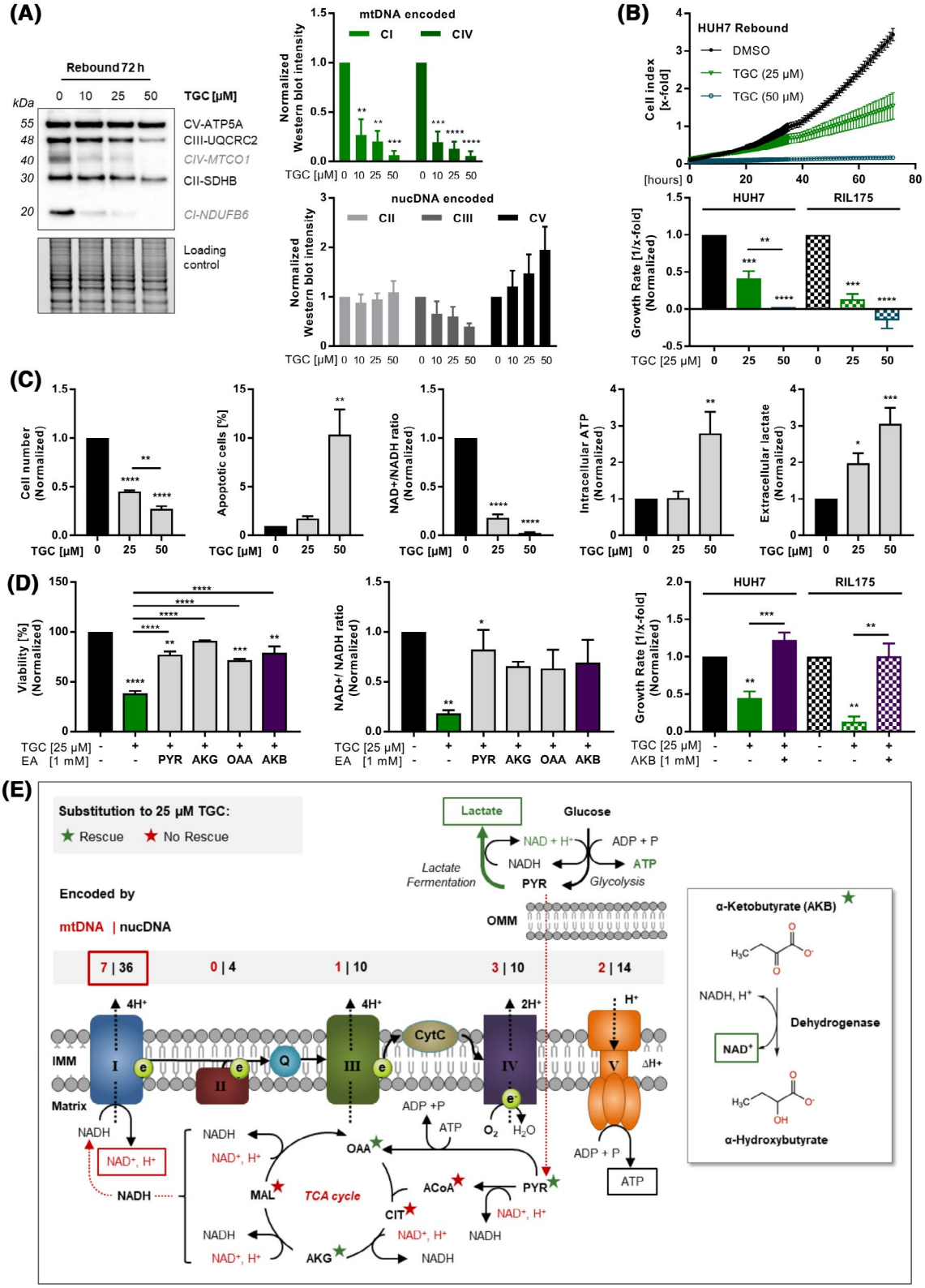

FIGURE 5 TGC impairs rebound growth by inhibiting TCA cycle activity. A, TGC inhibits the biogenesis of mtDNA-encoded ETS subunits. Immunoblot quantification of HUH7-R cells treated with TGC upon 72 hours of sorafenib withdrawal (ANOVA). B, TGC prevents rebound growth of HUH7-R and RIL175-R cells. Proliferation was assessed by impedance measurement (shown for HUH7-R; top). Growth rates of HUH7-R and RIL175-R cells were calculated from normalized cell counts (index) after 72 hours of TGC treatment (ANOVA). C, TGC inhibits TCA cycle and NDUF activity. Assessment of proliferation by crystal violet staining, apoptosis (percentage of total cell count), NAD^+/NADH ratio, intracellular ATP, and extracellular lactate, is shown. HUH7-R cells upon rebound growth were treated with TGC for 72 hours (ANOVA). D, Substitution with NAD^+-regenerating electron acceptors (EAs) rescues rebound growth. Viability (left) and NAD^+/NADH-ratio (middle) of HUH7-R cells treated with TGC upon 72 hours of sorafenib withdrawal and substituted with the respective EA is shown. Viability was obtained by subtracting the metabolite-specific toxicity when applied as a single treatment (Figure S6D). Growth rates (right) of HUH7-R and RIL175-R cells were assessed by impedance measurements over 72 hours of rebound growth (Figure S7D) (ANOVA). E, TGC impairs NAD^+ turnover and TCA cycle activity. The ETS is constantly powered by NADH turnover of the TCA cycle. A decrease in biogenesis of mtDNA-encoded Complex I subunits by TGC impairs NADH oxidation, leading to decreased TCA cycle activity and extracellular lactate fermentation. Substitution with extracellular EAs restores intracellular NAD^+ and rescues rebound growth, as they are substrates of intracellular dehydrogenases. All experiments were normalized to the untreated control. Values are shown as ± SEM, N = 3, $*P < .05$, $**P < .01$, $***P < .001$, $****P < .0001$

3.7 | TGC significantly impairs tumor relapse as a second-line therapy after sorafenib treatment in vivo

To assess TGC as a second-line therapy in vivo, we established an ectopic tumor mouse xenograft with stably luciferase-expressing HUH7-R-LUC cells. As already shown in vitro, TGC treatment significantly prevented tumor relapse upon sorafenib withdrawal in vivo, with a tumor size as well as growth rate comparable to that of persistently sorafenib-treated mice; overall good tolerance was observed (Figure 7A-C).[46] The excised tumors were visually smaller in the TGC-treated group, with a mean weight of 58.4 mg/tumor compared to 246.7 mg/tumor of the untreated group (Figure 7D,E). Protein levels of citrate synthase and PGC-1α, which indicate alterations of mitochondrial mass and biogenesis, were significantly altered by sorafenib but not by TGC treatment in vivo (Figure S9A). The impact of TGC on the biogenesis of mtDNA-encoded subunits in vivo was supported by significantly reduced CI-NDUFB6 protein expression. Sorafenib withdrawal increased the abundance of the nucDNA-encoded CV-ATP5A subunit, as demonstrated in vitro, but had no effect on CI-NDUFB6 expression in vivo (Figures 7F, S9B). In contrast to previous in vitro studies, tumor relapse was accompanied by elevated levels of the TCA cycle enzymes OGDH and IDH2 (Figure S9C). A comparable ectopic tumor mouse xenograft implemented over 14 days showed a strong initial effect of TGC treatment (Figure S10A), though no alterations were observed in expression patterns of ETS subunits, OGDH, or IDH2 at the time of tumor excision (Figure S10B-E). We suggest that expression of these proteins underlies regulatory dynamics over the time of therapy with the strongest effectiveness of TGC in an early phase after sorafenib withdrawal. Altogether, these in vivo results are consistent with the in vitro findings presented above, indicating the biogenesis of mtDNA-encoded ETS subunits as a potential target for therapeutic intervention in a second-line setting of sorafenib-resistant HCC.

4 | DISCUSSION

Since the 1970s, the epidemic of HCC has spread beyond Eastern Asia, with almost a doubling of cases reported in the United States and Canada within the last two decades.[47] Currently, sorafenib is the standard of care for first-line therapy for advanced-stage HCC. Nonetheless, with only 2% of patients showing a partial response, sorafenib resistance and consequent tumor relapse represent a serious challenge for prolonging the OS of these patients. In this study, we aimed to unravel unknown mechanistic features of sorafenib resistance with a special focus on tumor growth resumption after sorafenib treatment termination. Both contribute to the low therapeutic benefit of sorafenib as well as to the frequent failure of first-line and second-line therapeutic approaches in clinical trials.[48] Thus, clarifying the molecular basis of acquired resistance and the tumor relapse could help to find new therapeutic options for advanced-stage HCC patients.

To this end, we developed a human HCC cell line with acquired resistance to sorafenib in a range equivalent to the serum concentration of patients on a recommended sorafenib intake of 400 mg, twice daily.[49] First, we showed that these HUH7-R(+) cells were highly refractory to any tested chemotherapeutic treatment but that they regained sensitivity when sorafenib was withdrawn. These cross-resistant HUH7-R(+) cells underwent EMT, a phenomenon that has previously been associated with sorafenib resistance and a poor OS.[50] EMT was triggered by activation of the PI3K/Akt axis, and therefore, reversible after sorafenib withdrawal.[7] Thus, we conclude that upon acquired resistance, a second-line therapy is beneficial in comparison to combination treatment with sorafenib.

Second, we observed that sorafenib withdrawal promotes rapid resumption of proliferation, caused by mitochondrial regeneration and a metabolic switch from glycolysis to respiration. This rebound growth phenomenon was previously described,[7,51] though the underlying metabolic mechanism has not been investigated thus far. Anaerobic glycolysis, as observed in HUH7-R(+) cells, is physiologically promoted by the PI3K/Akt pathway.[52,53] Nonetheless, sorafenib-induced ETS dysfunction renders HUH7-R(+) cells dependent on lactate fermentation and reduces biosynthesis of TCA

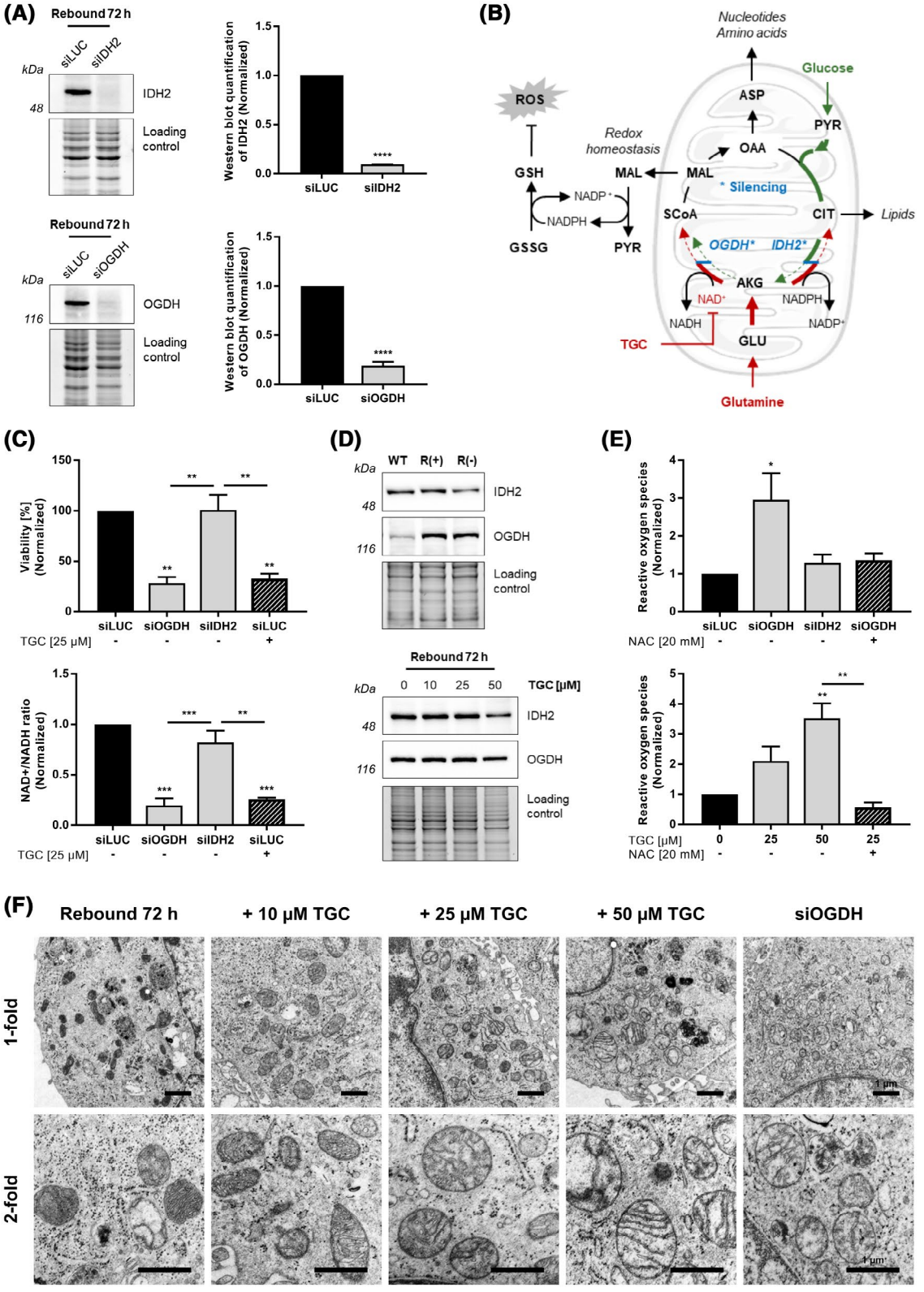

FIGURE 6 Glutamine oxidation is essential in tumor relapse and ROS defense. A, Transient gene silencing of IDH2 and OGDH upon rebound growth. Immunoblot analysis was normalized to the siLUC-transfected control (*t* test). B, Schematic illustration of the impact of IDH2 and OGDH silencing on glucose and glutamine metabolism and redox-mediated ROS production. C, OGDH silencing prevents tumor relapse by reducing NDUF activity. Viability and NAD^+/NADH-ratio were assessed in HUH7-R cells transiently transfected for 72 hours upon rebound growth and normalized to the siLUC transfected, untreated control (ANOVA). D, Increased protein expression of OGDH in HUH7-R cells. Immunoblot analysis of IDH2 and OGDH is shown (quantification: Figure S8A). E, Abrogated glutamine oxidation increases the ROS production. ROS levels were assessed in HUH7-R cells transiently transfected or treated with TGC for 72 hours upon rebound growth. The ROS scavenger N-acetyl cysteine (NAC) was used as a negative control, and ROS levels were normalized to the untreated, siLUC-transfected control (ANOVA). F, Abrogated glutamine oxidation promotes ROS-mediated mitochondrial damage. TEM of HUH7-R cells untreated, treated with TGC or transiently transfected with siOGDH upon 72 hours of rebound growth are shown. Scale bars indicate 1 μm. Values are shown as ± SEM, N = 3, $*P < .05$, $**P < .01$, $***P < .001$, $****P < .0001$

cycle metabolites required for anabolic processes, such as fatty acid synthesis.[45] Anaerobic glycolysis does not solely contribute to cell proliferation but is essentially limited by mtDNA maintenance and NDUF activity.[43,54] Therefore, we emphasize renewal of the ETS by mitochondrial biogenesis as a driving force for tumor relapse and as a potential target for therapeutic intervention after sorafenib failure.

Third, we efficiently prevented rebound growth by suppressing the biogenesis of mtDNA-encoded ETS subunits via treatment with the bacterial translation-inhibiting antibiotic TGC. To date, inhibition of mitochondrial biosynthesis by the use of antibiotics has not been investigated in HCC or as a chemotherapeutic second-line therapy in general. The targeted prokaryotic-derived mtDNA accounts for 13 essential subunits of the ETS and contributes to all metabolic functions, thus, we sought to determine which metabolite was rate limiting for rebound growth.[42,55] On the one hand, at high concentrations TGC enhanced CV-ATP5A expression and intracellular ATP levels, indicating that mitochondrial ATP generation may not be crucial. On the other hand, TGC impairs the NDUF-mediated oxidation of NADH to the electron acceptor NAD^+, required for driving aerobic TCA cycle activity to generate biosynthetic intermediates for lipids, nucleotides, and amino-acids.[53,56] The substitution experiments presented herein clearly demonstrated that TGC treatment establishes auxotrophy for exogenous electron acceptors that restore proliferation-limiting glutamine oxidation by regenerating NAD^+. It was shown that TGC thereby diminishes aspartate production, which plays an essential role in nucleotide biosynthesis and has been previously reported to limit proliferation under Complex I inhibition.[26] Aspartate can be generated by glutamate transamination and via reductive carboxylation or oxidative TCA cycle activity.[56] Nonetheless, aspartate substitution per se did not rescue the effect of TGC and aspartate levels are mostly restored by pyruvate, which can form aspartate by carboxylation and transamination independently of NAD^+.[26,45] The amino acids glutamate, cysteine and glycine, however, which are required for synthesis of the ROS-neutralizing tri-peptide glutathione, are all dependent on glutamine input.[45] In addition, abrogation of glutamine oxidation eliminates pools of malate and NADPH, both of which contribute to ROS elimination by glutathione reduction.[53] The mitochondrial $NADP^+$/NADPH ratio thereby reflects NDUF impairment by TGC via enzymatic hydride transfer from NADH to $NADP^+$, which is possibly compensated by evasive NADPH-consuming reductive carboxylation in OGDH-silenced HUH7-R cells.[57] In contrast, cytosolic NADPH levels essentially rely on TCA cycle-dependent malate turnover.[53] In summary, we could show that TGC treatment leads to electron acceptor depletion, which limits glutamine oxidation, required to promote rebound growth and to generate directly ROS-controlling products. Thus, inhibiting the biogenesis of the NAD^+-recycling NDUF may constitute a sensitive target for therapeutic intervention second-line to sorafenib. Importantly, translation-inhibiting antibiotics prevent the recurrence of tumor growth after sorafenib withdrawal, while enabling resensitization to long-term chemotherapeutic alternatives.

To date, there is scant research on the therapeutic benefit of antibiotics in cancer, as most studies focus on administration for cancer-associated infections. In initial endeavors, TGC was shown to selectively induce cell death in a panel of leukemia cell lines,[58] to target subtypes of lung and breast cancer[59,60] and to eradicate cancer stem cells.[61] TGC is a clinically approved low-cost antimicrobial agent that is used to treat complicated skin- and intraabdominal-infections.[62] Thus, TGC is characterized by a favorable safety profile and good experience in dosing schedules, with therefore tremendous promise for clinical translation. Herein, mitochondrial mass and biogenesis was not significantly altered by TGC treatment in vivo, suggesting low incidence of off-target side-effects mediated by altered mitochondrial dynamics. As translation-inhibiting antibiotics establish electron acceptor auxotrophy by impairing renewal of essential ETS subunits, we suggest good selectivity toward fast proliferating cancer cells and cells, which suffer mitochondrial damage due to previous chemotherapy. Given the metabolic implication for preventing the growth resumption in HUH7-R cells, we are the first to present the use of translation-inhibiting antibiotics as an efficacious second-line therapeutic approach for advanced-stage HCC patients.

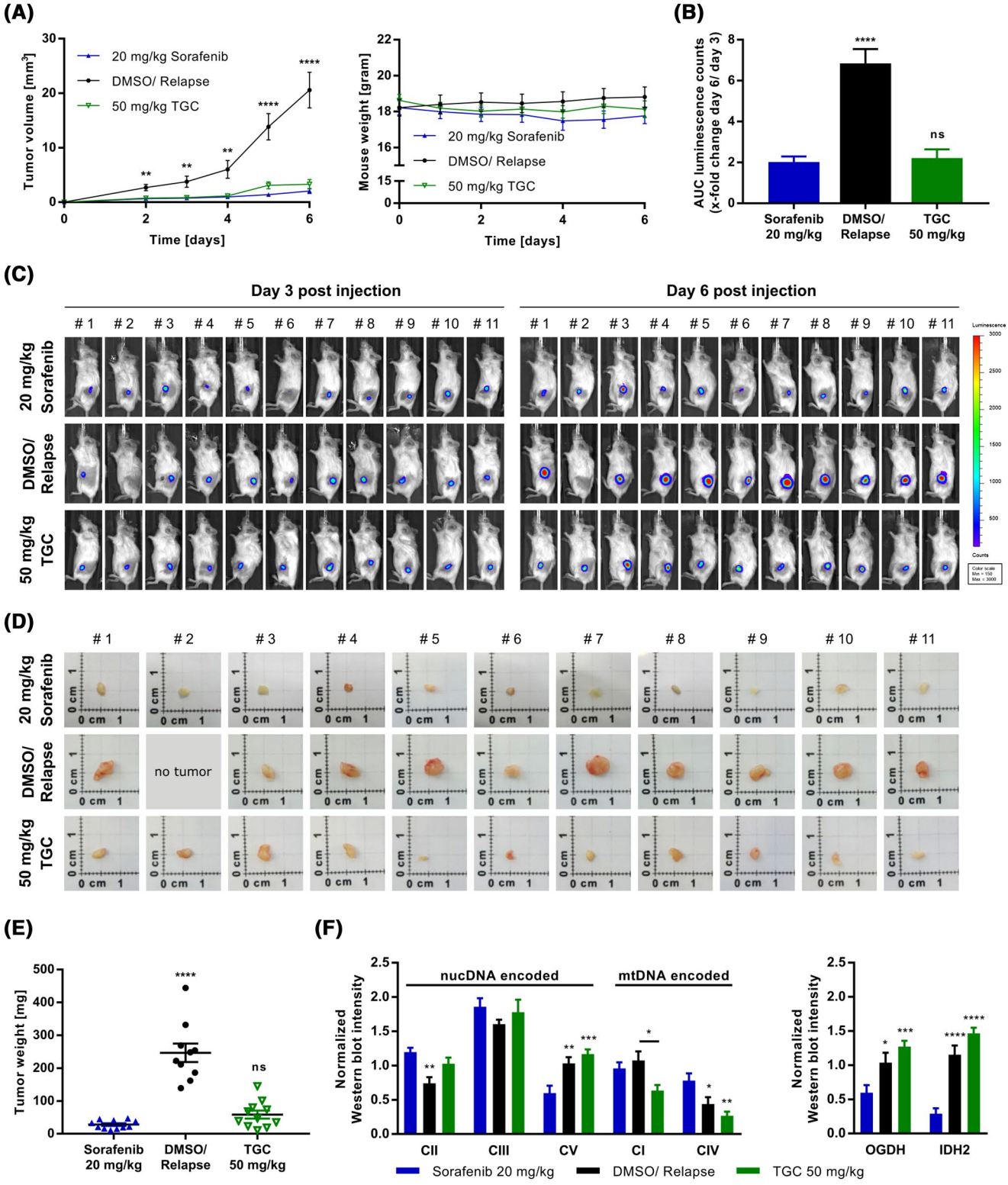

FIGURE 7 TGC prevents rebound growth after sorafenib treatment termination in vivo. A, TGC prevents tumor relapse in an ectopic tumor mouse xenograft of HUH7-R(+)-LUC cells. Mice were treated with 20 mg/kg sorafenib (Control), DMSO (Relapse), or 50 mg/kg TGC daily for 6 days. Control #2 was excluded because no tumor was detected until day 6 post-cell injection (ANOVA). B, TGC strongly reduces tumor growth rate as determined by in vivo bioluminescence imaging (day 6/ day 3). The AUC of luminescence counts was assessed for 20 minutes after 13 minutes of 0.3 g/kg luciferin injection (ANOVA). C, In vivo bioluminescence imaging at day 3 and day 6 of treatment. Images were taken 20 minutes after 0.3 g/kg luciferin injection (binning 4, min = 150 counts; max = 3000 counts). D, Images of excised tumors (Figure 7A). E, Weight of excised tumors (Figure 7D) (ANOVA). F, Significantly reduced CI-NDUFB6 protein expression upon TGC treatment in vivo. Immunoblot quantifications from excised tumors (Figure 7D) were normalized to the mean band intensity (ANOVA). Values are shown as ± SEM, N = 11, *$P < .05$, **$P < .01$, ***$P < .001$, ****$P < .0001$

ACKNOWLEDGMENTS

We thank Prof. Jeremias (Helmholtz Zentrum Munich, Germany) for providing the pCDH-eFFLuc-T2A-eGFP plasmid and Prof. Maria Kavallaris (University of New South Wales, Australia) for providing the CEM/VCR-R cells. We are grateful to Kerstin Loske (Ludwig-Maximilians-University Munich, Germany) and Pia Zaunmair (Paracelsus Medical Private University, Austria) for helping with the mouse experiments and Yaschar Kabiri (Technical University Munich, Germany) for sharing his experience on protein separation via tricine-PAGE. We acknowledge the DFG grant VO376/17-1 for AMV.

CONFLICT OF INTEREST

The authors declare no competing interests.

AUTHOR CONTRIBUTIONS

M. Meßner conceived and designed the study, performed in vitro proliferation, flow cytometric, metabolic, RT-PCR, and immunoblot experiments, performed immuno- and live cell staining, performed Perseus and GSEA analysis of proteomics data, helped with mouse experiments, analyzed all data and drafted the manuscript. S. Schmitt helped to design the study, performed TEM microscopy, and helped with high-resolution respirometry. M. A. Ardelt helped to design the study and generated the HUH7-R and RIL-R cell lines. S. Schmitt and M. A. Ardelt contributed equally. T. Fröhlich and G. J. Arnold performed the LC MS/MS-proteomics screen and subsequent MaxQuant analysis. M. Müller performed the glycolytic stress tests. H. Pein and A. Koeberle performed LC-MS/MS lipidomics with subsequent analysis. P. Huber-Cantonati and C. Ortler performed mouse experiments. L. M. Koenig and S. Rothenfußer helped with lentiviral transfection to generate the HUH7-R-LUC cell line. L. Zobel measured mitochondrial and lysosomal mass distributions. A. K. Kiemer provided conceptual advice. A. Gerbes helped to draft the manuscript. H. Zischka helped to design the study and had the initial idea to investigate antibiotics in the tumor relapse setting. A. M. Vollmar and J. Pachmayr helped to design the study, to draft the manuscript, and provided conceptual advice and support.

DATA AVAILABILITY STATEMENT

All data generated or analyzed during this study are included in the manuscript and supporting files. Mass spectrometry-derived source data (proteomics and lipidomics) used to generate Figures 2A,B and 4F are deposited online on *Mendeley Data*: https://doi.org/10.17632/t5z8v7752m.1. The processed data of the proteomics screening are provided in Figure S3B-D. Materials and reagents are available from the corresponding author on request. All Supporting Information including a table of the key resources with Research Resource Identifiers (RRIDs) is available online on The FASEB Journal's web site.

REFERENCES

1. Ferlay J, Soerjomataram I, Dikshit R, et al. Cancer incidence and mortality worldwide: sources, methods and major patterns in GLOBOCAN 2012. *Int J Cancer*. 2015;136:E359-386.
2. Gerbes A, Zoulim F, Tilg H, et al. Gut roundtable meeting paper: selected recent advances in hepatocellular carcinoma. *Gut*. 2018;67:380-388.
3. Bruix J, Reig M, Sherman M. Evidence-based diagnosis, staging, and treatment of patients with hepatocellular carcinoma. *Gastroenterology*. 2016;150:835-853.
4. Wilhelm SM, Carter C, Tang L, et al. BAY 43–9006 exhibits broad spectrum oral antitumor activity and targets the RAF/MEK/ERK pathway and receptor tyrosine kinases involved in tumor progression and angiogenesis. *Can Res*. 2004;64:7099-7109.
5. Llovet JM, Ricci S, Mazzaferro V, et al. Sorafenib in advanced hepatocellular carcinoma. *N Engl J Med*. 2008;359:378-390.
6. Cheng A-L, Kang Y-K, Chen Z, et al. Efficacy and safety of sorafenib in patients in the Asia-Pacific region with advanced hepatocellular carcinoma: a phase III randomised, double-blind, placebo-controlled trial. *Lancet Oncol*. 2009;10:25-34.
7. van Malenstein H, Dekervel J, Verslype C, et al. Long-term exposure to sorafenib of liver cancer cells induces resistance with epithelial-to-mesenchymal transition, increased invasion and risk of rebound growth. *Cancer Lett*. 2013;329:74-83.
8. Abdel-Aziz AK, Abdel-Naim AB, Shouman S, Minucci S, Elgendy M. From resistance to sensitivity: insights and implications of biphasic modulation of autophagy by sunitinib. *Front Pharmacol*. 2017;8:718.
9. Kudo M, Finn RS, Qin S, et al. Lenvatinib versus sorafenib in first-line treatment of patients with unresectable hepatocellular carcinoma: a randomised phase 3 non-inferiority trial. *Lancet (London, England)*. 2018;391:1163-1173.
10. Raoul J-L, Kudo M, Finn RS, Edeline J, Reig M, Galle PR. Systemic therapy for intermediate and advanced hepatocellular carcinoma: sorafenib and beyond. *Cancer Treat Rev*. 2018;68:16-24.
11. Kudo M. Immuno-oncology therapy for hepatocellular carcinoma: current status and ongoing trials. *Liver Cancer*. 2019;8:221-238.
12. Bruix J, Qin S, Merle P, et al. Regorafenib for patients with hepatocellular carcinoma who progressed on sorafenib treatment (RESORCE): a randomised, double-blind, placebo-controlled, phase 3 trial. *Lancet*. 2017;389:56-66.
13. El-Khoueiry AB, Sangro B, Yau T, et al. Nivolumab in patients with advanced hepatocellular carcinoma (CheckMate 040): an open-label, non-comparative, phase 1/2 dose escalation and expansion trial. *Lancet*. 2017;389:2492-2502.
14. Finkelmeier F, Waidmann O, Trojan J. Nivolumab for the treatment of hepatocellular carcinoma. *Expert Rev Anticancer Ther*. 2018;18:1169-1175.
15. Kapanadze T, Gamrekelashvili J, Ma C, et al. Regulation of accumulation and function of myeloid derived suppressor cells in different murine models of hepatocellular carcinoma. *J Hepatol*. 2013;59:1007-1013.
16. Haber M, Norris MD, Kavallaris M, et al. Atypical multidrug resistance in a therapy-induced drug-resistant human leukemia cell line (LALW-2): resistance to Vinca alkaloids independent of P-glycoprotein. *Can Res*. 1989;49:5281-5287.
17. Koeberle A, Shindou H, Koeberle SC, Laufer SA, Shimizu T, Werz O. Arachidonoyl-phosphatidylcholine oscillates during the cell cycle and counteracts proliferation by suppressing Akt membrane binding. *Proc Natl Acad Sci*. 2013;110:2546-2551.

18. Glatzel DK, Koeberle A, Pein H, et al. Acetyl-CoA carboxylase 1 regulates endothelial cell migration by shifting the phospholipid composition. *J Lipid Res*. 2018;59:298-311.
19. Bolte S, Cordelières FP. A guided tour into subcellular colocalization analysis in light microscopy. *J Microsc*. 2006;224: 213-232.
20. Manders EM, Stap J, Brakenhoff GJ, van Driel R, Aten JA. Dynamics of three-dimensional replication patterns during the S-phase, analysed by double labelling of DNA and confocal microscopy. *J Cell Sci*. 1992;103(Pt 3):857-862.
21. Nicoletti I, Migliorati G, Pagliacci MC, Grignani F, Riccardi C. A rapid and simple method for measuring thymocyte apoptosis by propidium iodide staining and flow cytometry. *J Immunol Methods*. 1991;139:271-279.
22. Laemmli UK. Cleavage of structural proteins during the assembly of the head of bacteriophage T4. *Nature*. 1970;227:680.
23. Schagger H. Tricine-SDS-PAGE. *Nat Protoc*. 2006;1:16-22.
24. Bradford MM. A rapid and sensitive method for the quantitation of microgram quantities of protein utilizing the principle of protein-dye binding. *Anal Biochem*. 1976;72:248-254.
25. Strumberg D, Clark JW, Awada A, et al. Safety, pharmacokinetics, and preliminary antitumor activity of sorafenib: a review of four phase I trials in patients with advanced refractory solid tumors. *Oncologist*. 2007;12:426-437.
26. Sullivan LB, Gui DY, Hosios AM, et al. Supporting aspartate biosynthesis is an essential function of respiration in proliferating cells. *Cell*. 2015;162:552-563.
27. Vander Heiden MG, Cantley LC, Thompson CB. Understanding the Warburg effect: the metabolic requirements of cell proliferation. *Science*. 2009;324:1029-1033.
28. Curi R, Newsholme P, Newsholme EA. Metabolism of pyruvate by isolated rat mesenteric lymphocytes, lymphocyte mitochondria and isolated mouse macrophages. *Biochem J*. 1988;250:383-388.
29. Warburg O. On the origin of cancer cells. *Science*. 1956;123:309-314.
30. Shen YC, Ou DL, Hsu C, et al. Activating oxidative phosphorylation by a pyruvate dehydrogenase kinase inhibitor overcomes sorafenib resistance of hepatocellular carcinoma. *Br J Cancer*. 2012;108:72-81.
31. Archer SL. Mitochondrial dynamics—Mitochondrial fission and fusion in human diseases. *N Engl J Med*. 2013;369:2236-2251.
32. Murphy MP. How mitochondria produce reactive oxygen species. *Biochem J*. 2009;417:1-13.
33. Holz MS, Janning A, Renne C, Gattenlohner S, Spieker T, Brauninger A. Induction of endoplasmic reticulum stress by sorafenib and activation of NF-kappaB by lestaurtinib as a novel resistance mechanism in Hodgkin lymphoma cell lines. *Mol Cancer Ther*. 2013;12:173-183.
34. Ma MKF, Lau EYT, Leung DHW, et al. Stearoyl-CoA desaturase regulates sorafenib resistance via modulation of ER stress-induced differentiation. *J Hepatol*. 2017;67:979-990.
35. Pickles S, Vigie P, Youle RJ. Mitophagy and quality control mechanisms in mitochondrial maintenance. *Curr Biol*. 2018;28:R170-R185.
36. Sugiura A, McLelland GL, Fon EA, McBride HM. A new pathway for mitochondrial quality control: mitochondrial-derived vesicles. *EMBO J*. 2014;33:2142-2156.
37. Tanaka A, Cleland MM, Xu S, et al. Proteasome and p97 mediate mitophagy and degradation of mitofusins induced by Parkin. *J Cell Biol*. 2010;191:1367-1380.
38. Ventura-Clapier R, Garnier A, Veksler V. Transcriptional control of mitochondrial biogenesis: the central role of PGC-1alpha. *Cardiovasc Res*. 2008;79:208-217.
39. LeBleu VS, O'Connell JT, Gonzalez Herrera KN, et al. PGC-1alpha mediates mitochondrial biogenesis and oxidative phosphorylation in cancer cells to promote metastasis. *Nat Cell Biol*. 2014;16(992–1003):1001-1015.
40. Dudek J. Role of cardiolipin in mitochondrial signaling pathways. *Front Cell Dev Biol*. 2017;5:90. https://doi.org/10.3389/fcell.2017.00090
41. Sagan L. On the origin of mitosing cells. *J Theor Biol*. 1967;14:255-274.
42. Taanman JW. The mitochondrial genome: structure, transcription, translation and replication. *Biochem Biophys Acta*. 1999;1410:103-123.
43. King M, Attardi G. Human cells lacking mtDNA: repopulation with exogenous mitochondria by complementation. *Science*. 1989;246:500-503.
44. Fan J, Kamphorst JJ, Mathew R, et al. Glutamine-driven oxidative phosphorylation is a major ATP source in transformed mammalian cells in both normoxia and hypoxia. *Mol Syst Biol*. 2013;9(1):712.
45. Altman BJ, Stine ZE, Dang CV. From Krebs to clinic: glutamine metabolism to cancer therapy. *Nat Rev Cancer*. 2016;16:619-634.
46. Gardiner D, Dukart G, Cooper A, Babinchak T. Safety and efficacy of intravenous tigecycline in subjects with secondary bacteremia: pooled results from 8 phase III clinical trials. *Clin Infect Dis*. 2010;50:229-238.
47. El-Serag HB. Epidemiology of viral hepatitis and hepatocellular carcinoma. *Gastroenterology*. 2012;142:1264-1273.e1261.
48. Kudo M. Lenvatinib in advanced hepatocellular carcinoma. *Liver Cancer*. 2017;6:253-263.
49. Al-Rajabi R, Patel S, Ketchum NS, et al. Comparative dosing and efficacy of sorafenib in hepatocellular cancer patients with varying liver dysfunction. *J Gastrointest Oncol*. 2015;6:259-267.
50. Zhang L, Zhou F, ten Dijke P. Signaling interplay between transforming growth factor-beta receptor and PI3K/AKT pathways in cancer. *Trends Biochem Sci*. 2013;38:612-620.
51. Ebos JML, Pili R. Mind the gap: potential for rebounds during anti-angiogenic treatment breaks. *Clin Cancer Res*. 2012;18:3719-3721.
52. Elstrom RL, Bauer DE, Buzzai M, et al. Akt stimulates aerobic glycolysis in cancer cells. *Can Res*. 2004;64:3892-3899.
53. DeBerardinis RJ, Lum JJ, Hatzivassiliou G, Thompson CB. The biology of cancer: metabolic reprogramming fuels cell growth and proliferation. *Cell Metab*. 2008;7:11-20.
54. Wheaton WW, Weinberg SE, Hamanaka RB, et al. Metformin inhibits mitochondrial complex I of cancer cells to reduce tumorigenesis. *eLife*. 2014;3. https://doi.org/10.7554/eLife.02242
55. Scarpulla RC. Nuclear control of respiratory gene expression in mammalian cells. *J Cell Biochem*. 2006;97:673-683.
56. Birsoy K, Wang T, Chen W, Freinkman E, Abu-Remaileh M, Sabatini DM. An essential role of the mitochondrial electron transport chain in cell proliferation is to enable aspartate synthesis. *Cell*. 2015;162:540-551.
57. Mullen AR, Hu Z, Shi X, et al. Oxidation of alpha-ketoglutarate is required for reductive carboxylation in cancer cells with mitochondrial defects. *Cell Rep*. 2014;7:1679-1690.
58. Skrtic M, Sriskanthadevan S, Jhas B, et al. Inhibition of mitochondrial translation as a therapeutic strategy for human acute myeloid leukemia. *Cancer Cell*. 2011;20:674-688.

59. Jones RA, Robinson TJ, Liu JC, et al. RB1 deficiency in triple-negative breast cancer induces mitochondrial protein translation. *J Clin Investig*. 2016;126:3739-3757.
60. Jia X, Gu Z, Chen W, Jiao J. Tigecycline targets nonsmall cell lung cancer through inhibition of mitochondrial function. *Fundam Clin Pharmacol*. 2016;30:297-306.
61. Lamb R, Ozsvari B, Lisanti CL, et al. Antibiotics that target mitochondria effectively eradicate cancer stem cells, across multiple tumor types: treating cancer like an infectious disease. *Oncotarget*. 2015;6:4569-4584.
62. Bradford PA, Weaver-Sands DT, Petersen PJ. In vitro activity of tigecycline against isolates from patients enrolled in phase 3 clinical trials of treatment for complicated skin and skin-structure infections and complicated intra-abdominal infections. *Clin Infect Dis*. 2005;41(Suppl 5):S315-S332.

SUPPORTING INFORMATION

Additional Supporting Information may be found online in the Supporting Information section.

How to cite this article: Meßner M, Schmitt S, Ardelt MA, et al. Metabolic implication of tigecycline as an efficacious second-line treatment for sorafenib-resistant hepatocellular carcinoma. *The FASEB Journal*. 2020;34:11860–11882. https://doi.org/10.1096/fj.202001128R